

NEW RESULTS ON CLEO'S HEAVY QUARKS — BOTTOM AND CHARM

Scott Menary

University of California, Santa Barbara
menary@charm.physics.ucsb.edu

Representing the CLEO Collaboration

ABSTRACT

While the top quark is confined to virtual reality for CLEO, the increased luminosity of the Cornell Electron Storage Ring (CESR) and the improved photon detection capabilities of the CLEO II detector have allowed for a rich program in the physics of CLEO's "heavy" quarks — bottom and charm. I will describe new results in the B meson sector including the first observation of exclusive $b \rightarrow u\ell\nu$ decays, upper limits on gluonic penguin decay rates, and precise measurements of semileptonic and hadronic $b \rightarrow c$ branching fractions. The charmed hadron results that are discussed include the observation of isospin violation in D_s^{*+} decays, an update on measurements of the D_s^+ decay constant, and the observation of a new excited Ξ_c charmed baryon. These measurements have had a large impact on our understanding of heavy quark physics.

1 Introduction

The central goal of heavy flavor physics below the top quark threshold is to measure the elements of the Cabibbo-Kobayashi-Maskawa (CKM) Matrix, since it is the Standard Model prescription for \mathcal{CP} Violation. This can be accomplished through measuring a multitude of b hadron decay rates and time-dependent decay asymmetries. Besides being interesting in and of itself, charmed hadron physics is also relevant to B decays through being a laboratory where many of the questions regarding QCD effects in heavy flavor decay can be addressed. After a short description of the experimental considerations of doing physics at the $\Upsilon(4S)$, I will describe a host of B meson and charmed hadron measurements done by CLEO in the last half-year.¹ I will also try to give some feel for the implications of these measurements towards our understanding of heavy flavor physics.

2 CLEO and CESR

At CESR, the highest luminosity collider in the world, the electron and positron beam energies are set to perform physics in the region of the Υ resonances, the system of $b\bar{b}$ bound states. The hadronic e^+e^- cross-section in this center-of-mass region is shown in Fig. 1. All the Υ resonances lower in mass than the $\Upsilon(4S)$ are

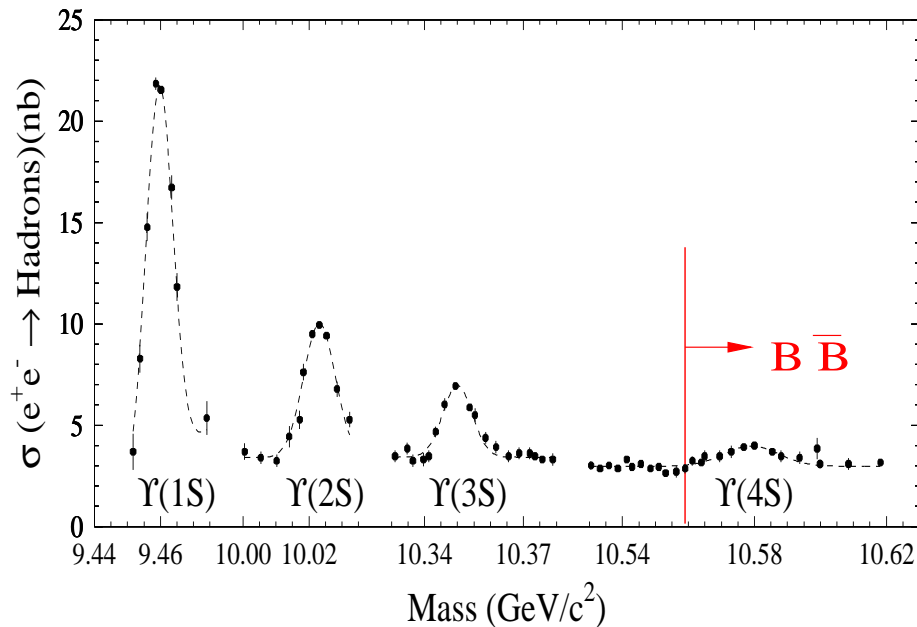


Figure 1: The e^+e^- cross-section in the Υ region.

below threshold for producing a $B\bar{B}$ pair. The cross-section at the $\Upsilon(4S)$ is about a nanobarn above the “continuum” cross-section of ~ 3.4 nb, and $c\bar{c}$ production constitutes about a nanobarn of the continuum. Hence, every fb^{-1} of data taken at the $\Upsilon(4S)$ contains about 10^6 $B\bar{B}$ and $c\bar{c}$ pairs. Further, the b quark decays essentially 100% of the time to a c quark giving another million charmed particles per fb^{-1} . The CLEO data sample to date consists of 3.3 fb^{-1} of data taken at the $\Upsilon(4S)$ resonance (so-called “on-resonance” data) and about half as much taken at an energy below the $B\bar{B}$ threshold (referred to as “continuum” or “off-resonance” data). The results discussed in this paper are based on about two-thirds of this data.

The CLEO II detector, shown in a cutaway r - z view in Fig. 2, measures both charged and neutral particles with excellent efficiency and resolution.²

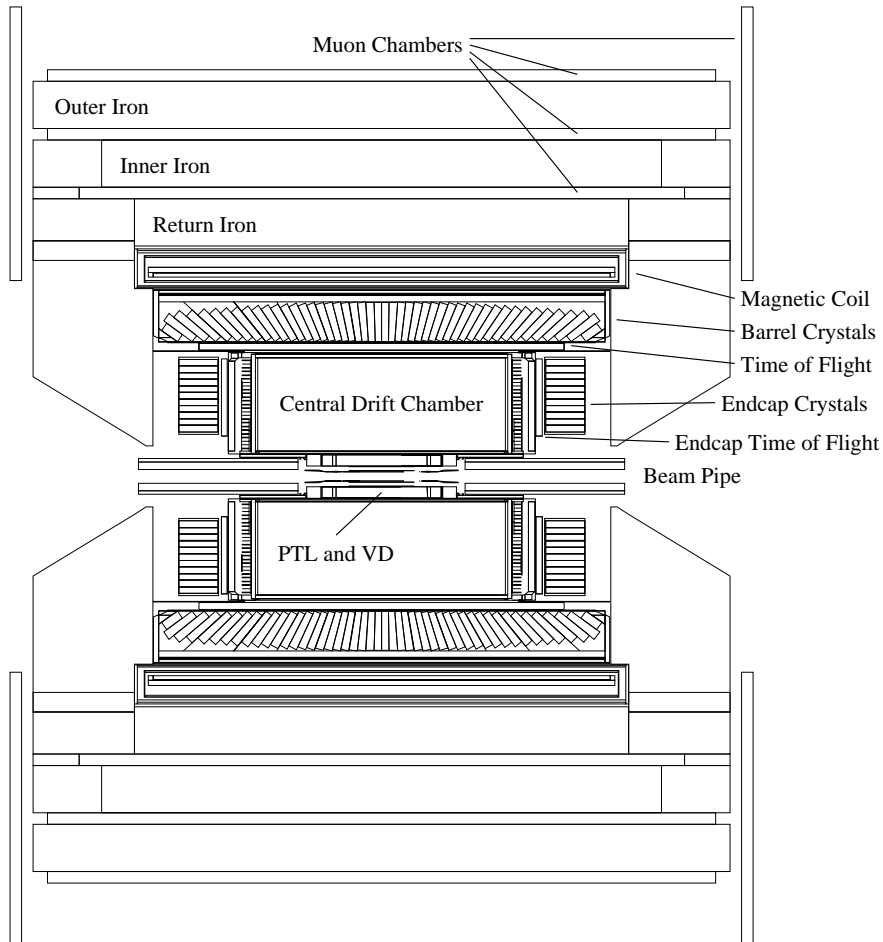


Figure 2: An r - z view of the CLEO II detector. For scale, the Time of Flight (TOF) system is at a radius of ~ 1 meter.

The tracking detectors, the TOF system, and the CsI calorimeter are located inside the 1.5 Tesla magnetic field. Analyses requiring good lepton identification or maximal photon energy resolution generally restrict the candidate particles to having been detected in the “barrel” part of the detector (i.e., $\cos \theta < 0.71$ where θ is the angle between the particle’s momentum and the beam axis). Most analyses have a minimum electron momentum requirement of ~ 600 MeV while the detector is only efficient for muons above about 1 GeV. Photons of energy down to 30 MeV are used while the charged tracking efficiency turns on at around 50 MeV and plateaus in the mid- to high-90th percentile, depending on particle type and track quality requirements. Particle identification is done using dE/dx measurements in the main drift chamber and the TOF system. This provides greater than 2σ K - π separation up to about 1 GeV, with much better separation than this from dE/dx up to about 700 MeV, and around 1.8σ separation at 2.4 GeV, the momentum region of interest for charmless hadronic B decay searches.

There are several unique aspects of doing physics at the $\Upsilon(4S)$ which make it especially good for studying B mesons and charmed hadrons. First, considering B meson production, since the $\Upsilon(4S)$ is just above the threshold for producing $B\bar{B}$, there are no B^* , B_s , or Λ_b hadrons produced, nor are there any extra particles produced along with the $B\bar{B}$ pair. This leads to the very powerful constraint that the B meson energy is equal to the beam energy. This can be used to select B meson candidates by requiring that ΔE , the difference between the measured sum of the charged and neutral energies of the daughters of the B candidate and the beam energy, be close to zero. Also, the B mass resolution is greatly improved by using the beam-constrained mass (M_B), defined by:

$$M_B^2 = E_{beam}^2 - \left(\sum_i \vec{p}_i \right)^2, \quad (1)$$

where \vec{p}_i is the momentum of the i -th daughter of the B candidate. The M_B resolution of about 2.6 MeV is determined by the beam energy spread and is a factor of ten better than the resolution in invariant mass obtained from simply summing the four-momenta of the B daughters.

Since the B mesons are produced almost at rest (the average B momentum is ~ 320 MeV), their decay products are uniformly distributed throughout the volume of the detector leading to events that tend to be “spherical” in shape, as illustrated in Fig. 3. Continuum $e^+e^- \rightarrow q\bar{q}$ ($q = u, d, s, c$) events are more

jet-like in structure, as shown in Fig. 4. Event shapes are utilized to distinguish $B\bar{B}$ events from continuum events. Charmed hadrons produced in the continuum can often be the largest source of background in B physics analyses at the $\Upsilon(4S)$ (the $B \rightarrow K^*\gamma$ analysis is an example of such) which is why some amount of data is taken below $B\bar{B}$ threshold so as to be able to study the characteristics of these events.

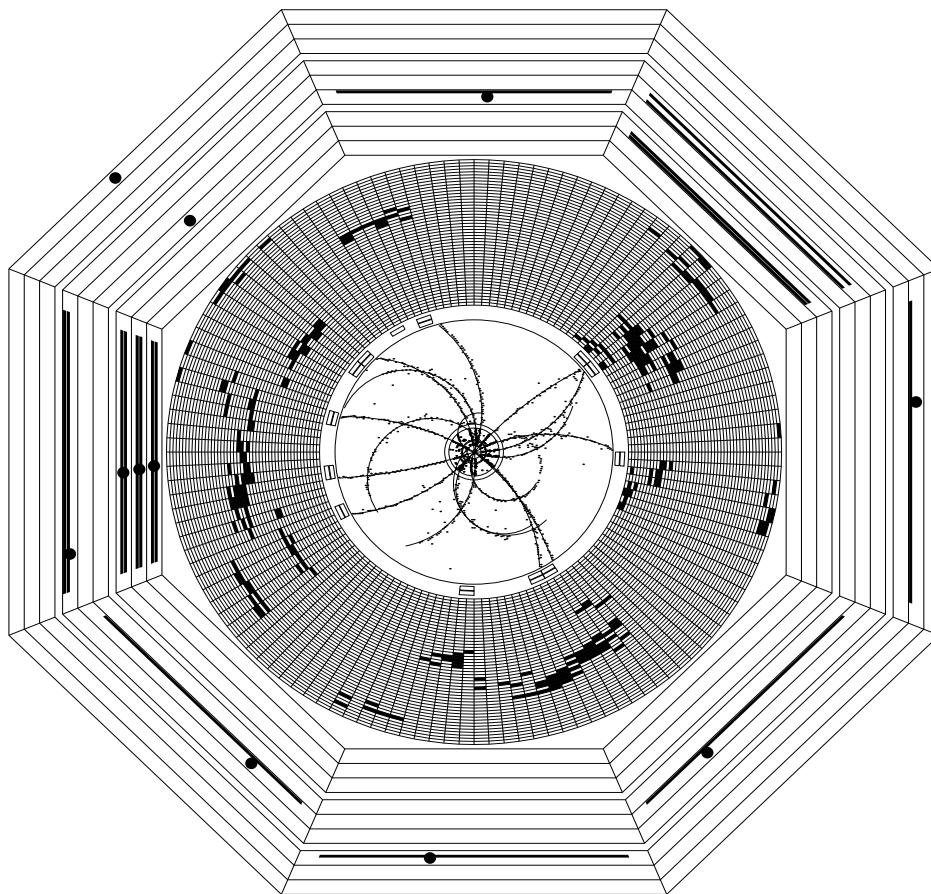


Figure 3: An r - ϕ view of a $B\bar{B}$ event in the CLEO II detector. See Figure 4 for a description of the display.

CleoXD

Run: 55422

Event: 22909

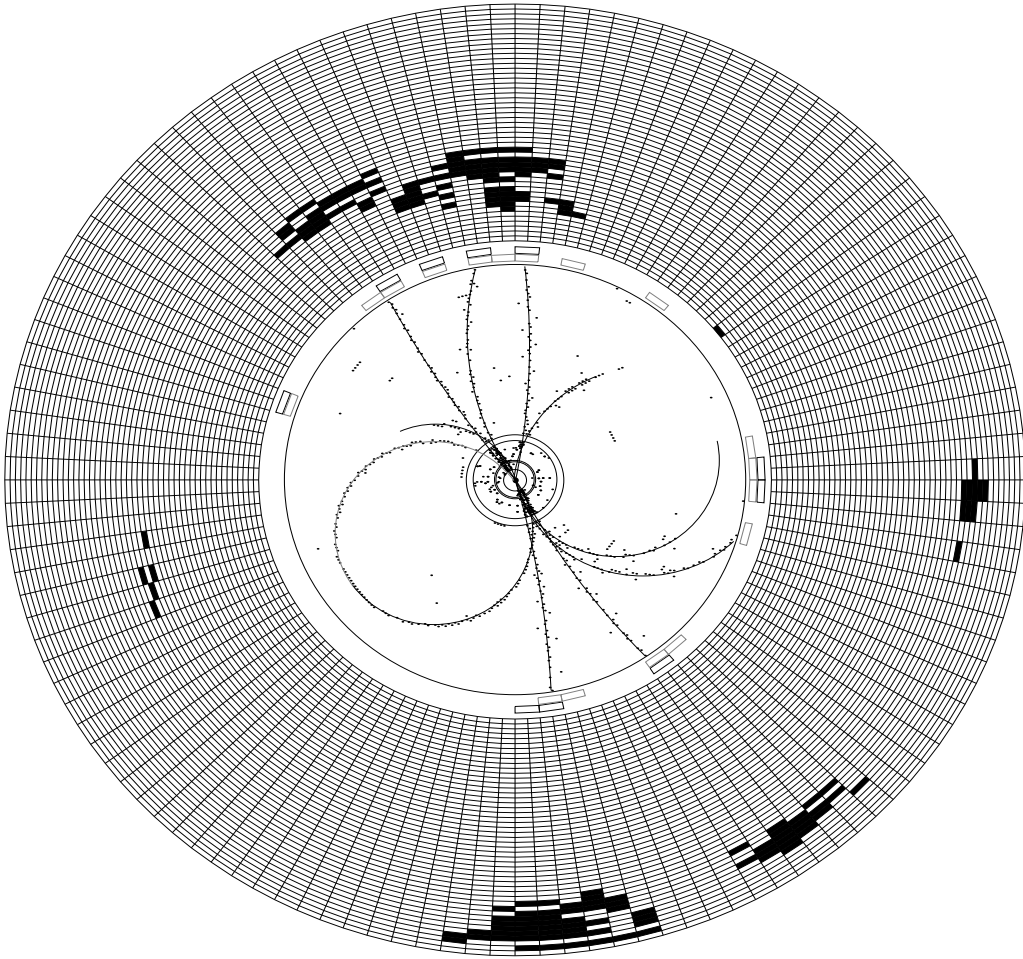


Figure 4: A fully reconstructed, off-resonance $e^+e^- \rightarrow \Lambda_c^- \pi^+ \pi^- \Lambda_c^{*+}(2593)$ event where the Λ_c^{*+} decayed to $\Lambda_c^+ \pi^+ \pi^-$ and both Λ_c 's decayed to $pK\pi$. Starting from the center are shown the hits and reconstructed tracks in the tracking devices. Outside of this is a thin annulus where hit TOF counters are shown as empty rectangles. Beyond this is a representation of the calorimeter which gives information in the z view as well. The crystals are shown as boxes where the inner radius is furthest from the viewer (in z) and the outer radius is closest. A crystal is blackened where an energy deposition above some threshold was measured. The muon counters (not shown here but in Figure 3) in the return yoke of the magnet are outside of the calorimeter.

3 Charmed Hadrons

In $e^+e^- \rightarrow c\bar{c}$ events at 10.58 GeV center-of-mass, the charmed hadron carries most of the charmed quark's energy (which is the beam energy). Conversely, the absolute kinematic cutoff for charmed hadrons from B decay is $m_B/2 \approx 2.5$ GeV. This is illustrated by the inclusive D_s^+ momentum spectrum in Fig. 5 where there is a clear demarcation in momentum between D_s^+ mesons produced in B decay and those from the continuum. Since the combinatorial background generally

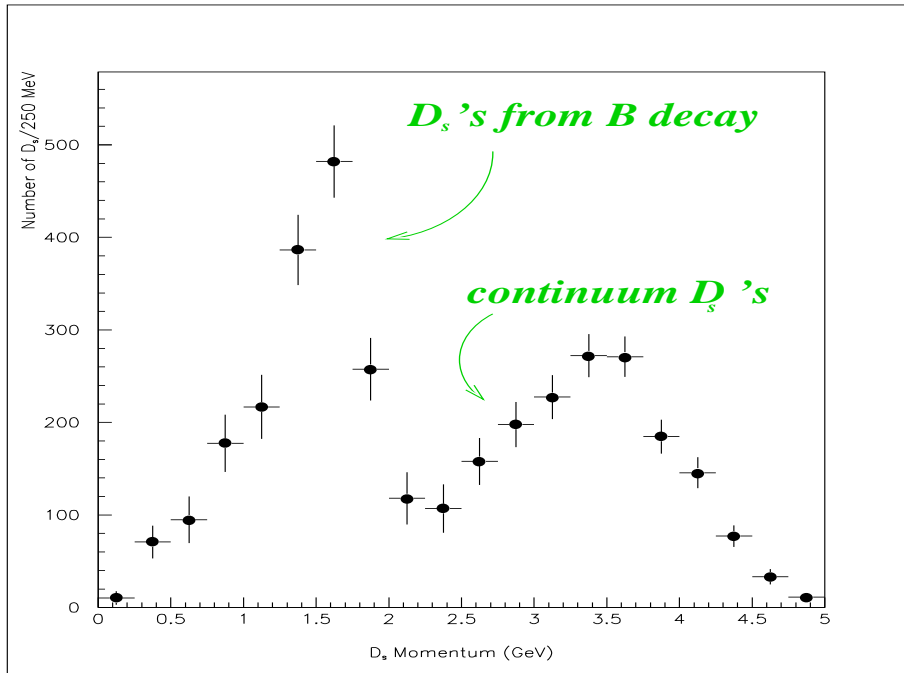


Figure 5: The D_s^+ momentum spectrum.

falls sharply with increasing momentum, most charm analyses require a minimum charmed hadron candidate momentum of 2.5 to 3 GeV.*

The discovery of the large lifetime difference between the D^+ and D^0 mesons was the first clue that charmed meson decays are much more complicated than the simple spectator picture would predict. In some senses, charmed baryons are even more interesting because, for example, the W -exchange diagram is not helicity suppressed. The fact that the Λ_c lifetime is about half that of the D^0 supports the view that interesting things are happening in charmed baryon hadronic decays.

*Another variable that is often used is $x \equiv p/p_{max}$ where $p_{max} = \sqrt{E_{beam}^2 - m_{hadron}^2}$. So, requiring $x > 0.5$ or 0.6 is equivalent to the momentum cut mentioned in the text.

3.1 Charmed Baryons — The Year of the Ξ_c

Last year CLEO published many new Λ_c results including: the observation of a new excited Λ_c ,³ measurements of semileptonic Λ_c decays,⁴ and the observation of new hadronic decay channels involving the η .⁵ This year has seen mostly new results on the Ξ_c , the csq baryon (where $q = u$ or d).

3.1.1 New Ξ_c Decay Modes

The CLEO result⁶ of $\tau(\Xi_c^+)/\tau(\Xi_c^0) = 2.46 \pm 0.70_{-0.23}^{+0.33}$ is another indication that it is going to take the observation of many different Ξ_c hadronic decay modes to untangle the relative strengths of the various diagrams involved in Ξ_c decay.[†] Simple spectator decay results in Ξ_c^+ decays to Ξ^0 , and CLEO reported previously on the observation of such decay modes.⁷ Other hyperons, such as the Σ^+ or Λ , are produced through more exotic decay mechanisms like internal W emission.

New CLEO results on Ξ_c^+ decays are given in Table 1. The Λ is reconstructed in its decay to $p\pi^-$ while the $p\pi^0$ channel is used to reconstruct the Σ^+ . The $\Sigma^+K^-\pi^+$ final state is found to be roughly 50% two-body $\Sigma^+\bar{K}^{*0}$ and 50% nonresonant.

Decay Mode	x_p cut	Events	\mathcal{E} (%)	$\mathcal{B}/\mathcal{B}(\Xi_c^+ \rightarrow \Xi^-\pi^+\pi^+)$
$\Sigma^+K^-\pi^+$	0.5	119 ± 23	10.4	$1.18 \pm 0.26 \pm 0.17$
$\Sigma^+\bar{K}^{*0}$	0.5	61 ± 17	9.8	$0.92 \pm 0.27 \pm 0.14$
$\Lambda K^-\pi^+\pi^+$	0.6	61 ± 15	11.5	$0.58 \pm 0.16 \pm 0.07$
$\Xi^-\pi^+\pi^+$	0.5	131 ± 14	10.6	1.0

Table 1: Summary of results on new Ξ_c^+ decay modes. The $\Sigma^+K^-\pi^+$ mode includes both resonant and non-resonant contributions. The efficiencies (\mathcal{E}) do not include branching fractions to the observed final states.

3.1.2 Observation of an Excited Ξ_c State

There are two Ξ_c states in which the sq diquark is in an $S = 1$ state — the Ξ_c' and Ξ_c^* with $J^P = \frac{1}{2}^+$ and $\frac{3}{2}^+$, respectively. The Ξ_c' is predicted to be below threshold

[†]It will be standard throughout this paper that the first error given on a result is statistical and the second is the systematic error. Also, when a hadron's charge is given, the charge conjugate hadron (or decay chain) is implicitly included unless otherwise stated.

for decaying to $\Xi_c \pi$ and so decays radiatively. The Ξ_c^* was expected to be just above threshold for the pionic decay giving hope that the width would be rather narrow, à la $D^* \rightarrow D\pi$. The signals for the Ξ_c^+ decay channels chosen for the Ξ_c^* search are shown in Fig. 6. These decay channels were selected based on the

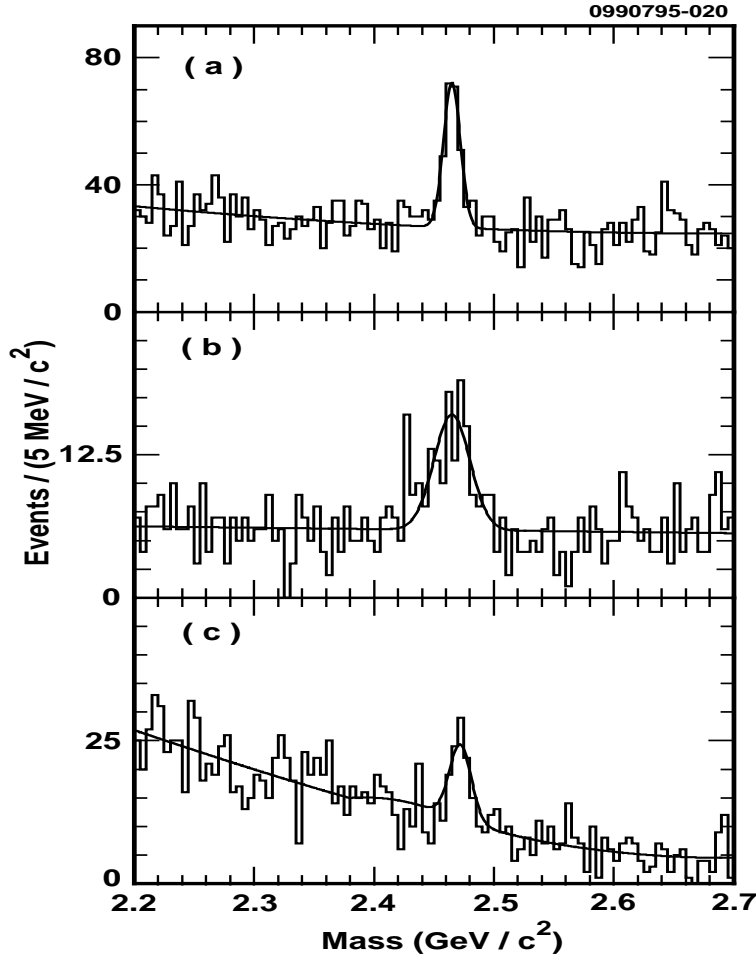


Figure 6: The Ξ_c^+ samples used in the Ξ_c^{*0} analysis. The Ξ_c^+ final states are: (a) $\Xi^- \pi^+ \pi^+$, (b) $\Xi^0 \pi^+ \pi^0$, and (c) $\Sigma^+ \bar{K}^{*0}$.

desire to have good signal to background before the addition of the extra pion. Note that the “new” $\Sigma^+ \bar{K}^{*0}$ mode is one of the channels. Also, the $\Xi^0 \pi^+ \pi^0, \Xi^0 \rightarrow \Lambda \pi^0, \Lambda \rightarrow p \pi^-$ decay chain is rather tricky since it involves the reconstruction of two detached vertices for the long-lived Ξ^0 and Λ , the first of which is a decay to two neutral particles.

The Ξ_c^+ candidates are then combined with each remaining π^- track and the mass difference, $M(\Xi_c^+ \pi^-) - M(\Xi_c^+)$, is calculated. The result is shown in Fig. 7 where a clear peak at threshold is evident. The signal function used to fit the

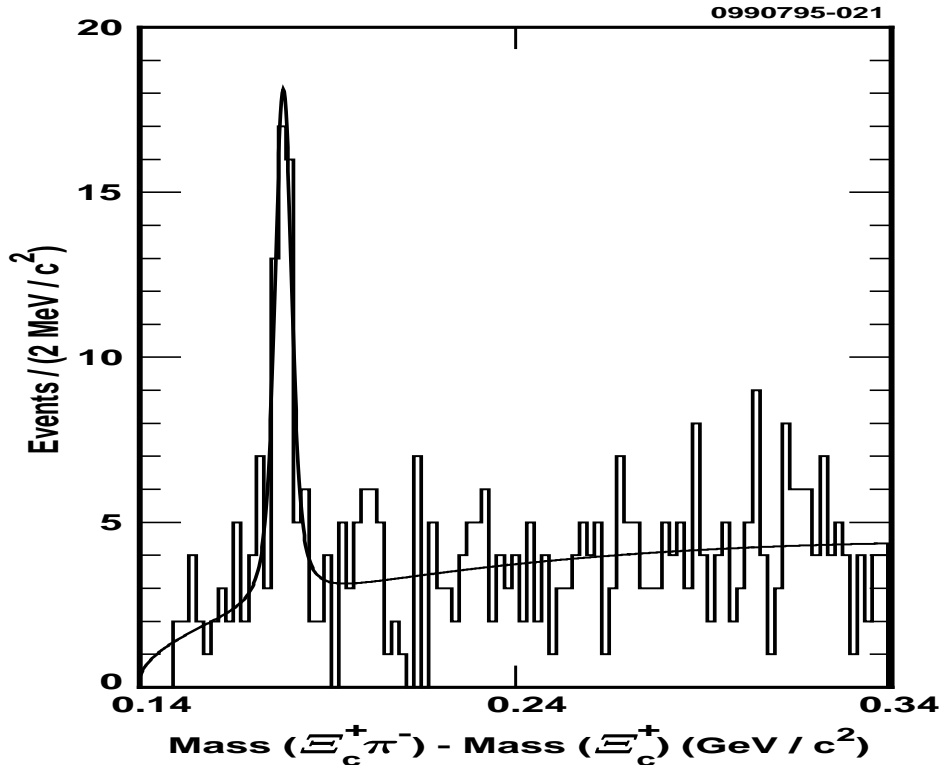


Figure 7: The $M(\Xi_c^+ \pi^-) - M(\Xi_c^+)$ data (histogram) and fit.

peak consisted of a Breit-Wigner convoluted with a Gaussian resolution function ($\sigma = 1.6$ MeV). The mass difference is found to be $178.2 \pm 0.5 \pm 1.0$ MeV, and the 90% confidence level upper limit on the width is 5.5 MeV. The mass and width of this new state are consistent with the theoretical predictions for the $J^P = \frac{3}{2}^+ \Xi_c^*$. It is found that a rather large fraction, $(27 \pm 6 \pm 6)\%$, of Ξ_c^+ baryons come from Ξ_c^{*0} decay.

3.2 Charmed Mesons — The Year of the D_s^+

This year saw a number of new and updated D_s^+ results from CLEO. A few of them are summarized in this section.

3.2.1 Observation of the Isospin-Violating Decay $D_s^{*+} \rightarrow D_s^+ \pi^0$

The D_s^{*+} has been observed exclusively in the $D_s^+ \gamma$ final state. The $D_s^{*+} \rightarrow D_s^+ \pi^0$ decay chain is kinematically allowed but is forbidden by isospin conservation. It was recently suggested by Cho and Wise⁸ that the isospin-violating decay could occur via the scenario where the D_s^{*+} decays to a D_s^+ and a virtual η (through

its $s\bar{s}$ component) which then mixes into a π^0 . This is illustrated in Fig. 8. The

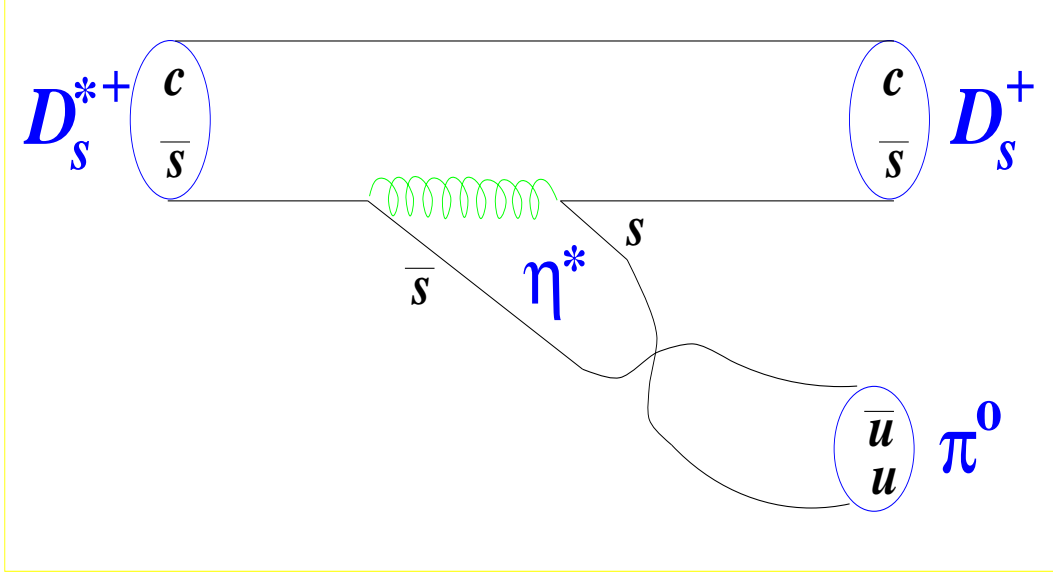


Figure 8: The diagram describing $D_s^{*+} \rightarrow D_s^+ \pi^0$ decay.

decay amplitude is proportional to the light quark masses in the combination $(m_d - m_u)/[m_s - (m_d + m_u)/2]$, which is zero in the limit of equal u and d quark masses (i.e., absolute isospin conservation). The prediction from Ref. 8 is that $R_0 \equiv \Gamma(D_s^{*+} \rightarrow D_s^+ \pi^0)/\Gamma(D_s^{*+} \rightarrow D_s^+ \gamma) \approx 0.01 - 0.10$.

The CLEO analysis of this decay mode starts with the “standard” $D_s^+ \rightarrow \phi \pi^+, \phi \rightarrow K^+ K^-$ decay chain which offers the best efficiency and signal-to-background (mostly because of the narrowness of the ϕ) of the many D_s^+ decay channels. The resulting peak after combining the D_s^+ candidates with each π^0 in the event is shown in Fig. 9. The significance of the peak, which contains $14.7^{+4.6}_{-4.0}$ events, is found to be greater than 3.9 standard deviations.

The major background is combinatorics since there are many random π^0 's in an event. Two “physics” backgrounds were found to be negligible. There is no contribution to the D_s^+ mass region from the $D^{*+} \rightarrow D^+ \pi^0, D^+ \rightarrow K^- \pi^+ \pi^+$ decay chain, where one of the pions is misidentified as a kaon, because of the requirement that the K^- and “false” K^+ reconstruct at the ϕ mass. Also, the possible background from $D_s^{*+} \rightarrow D_s^+ \gamma$ plus random photons was found to be negligible, both from a Monte Carlo study and in the data using $D_s^{*+} \rightarrow D_s^+ \gamma$ events.

The resulting value for R_0 is $0.062^{+0.020}_{-0.018} \pm 0.22$. If it is assumed that the two branching fractions sum to one, then the individual branching fractions are $\mathcal{B}(D_s^{*+} \rightarrow D_s^+ \pi^0) = 0.058^{+0.018}_{-0.016} \pm 0.020$ and $\mathcal{B}(D_s^{*+} \rightarrow D_s^+ \gamma) = 0.942^{+0.016}_{-0.018} \pm 0.020$. The width of the signal is entirely consistent with being due to detector resolution.

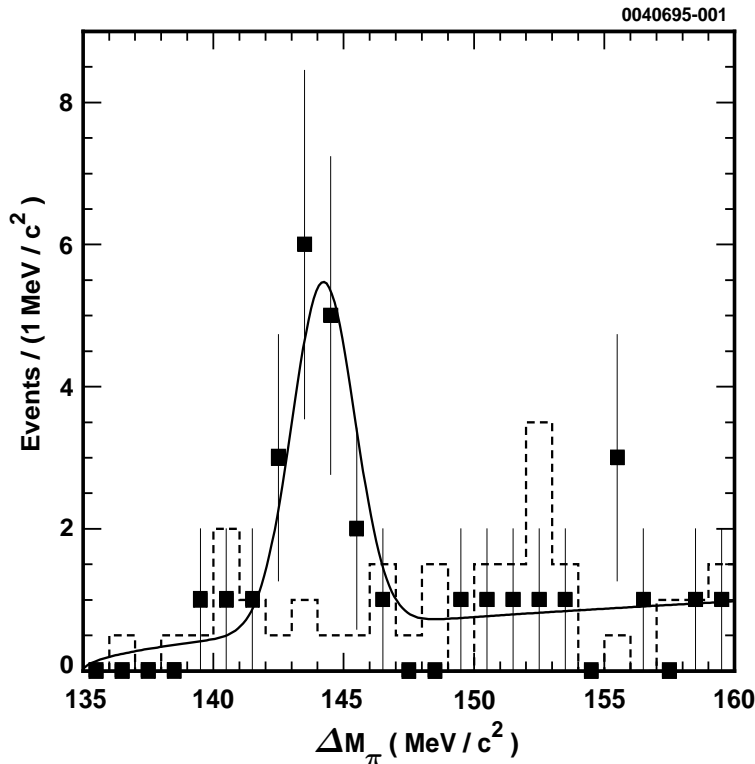


Figure 9: The $\Delta M_\pi \equiv M(D_s^+ \pi^0) - M(D_s^+)$ mass spectrum. The points are the data after all cuts, the solid line is the fit to the data, and the dashed line is an estimate of the background using D_s^+ and π^0 mass sidebands.

There are two other interesting results which follow from the observation of this isospin-violating decay mode. Conservation of spin and parity in the strong decay of the D_s^{*+} to two pseudoscalars means it must have natural spin-parity (0^+ , 1^- , 2^+ ...) and the radiative decay rules out 0^\pm . Thus, the most likely spin-parity assignment is $J^P = 1^-$, the same as for the D^{*+} and D^{*0} . Finally, even though this result is statistics limited, the mass difference resolution for the hadronic channel is so much better than for the radiative decay that the value for the mass difference measured using this decay is as precise as the published number from CLEO of $M(D_s^{*+}) - M(D_s^+) = 144.22 \pm 0.47 \pm 0.37$ MeV using the $D_s^{*+} \rightarrow D_s^+ \gamma$ channel. The

result for the hadronic channel is $M(D_s^{*+}) - M(D_s^+) = 143.76 \pm 0.39 \pm 0.40$ MeV, and the average of the two (they are statistically and systematically uncorrelated) is 143.97 ± 0.41 MeV.

3.2.2 Update on $D_s^+ \rightarrow \mu^+ \nu$ and f_{D_s} , the D_s^+ Decay Constant

Decay constants are a measure of the nonperturbative physics associated with quarks binding into mesons and are a source of great activity for those doing Lattice Gauge, QCD Sum Rules, and Quark Model calculations. Decay constants are important because they are often the largest source of uncertainty in extracting parameters of the Standard Model from measurements. For example, in $B^0 - \bar{B}^0$ mixing, the mixing parameter is given by:

$$x_d = \Delta M/\Gamma \propto V_{tb}^2 V_{td}^2 f_B^2 B_B m_t^2 F(m_t/m_W)^2$$

where F is a slowly varying function of m_t/m_W . With the present precision on m_t , the largest source of uncertainty in the extraction of V_{td} from measurements of x_d is the product of f_B , the B decay constant, and $\sqrt{B_B}$, where B_B is a parameter describing the degree to which the box diagrams dominate mixing. As another example, a calculation of the expected rate for the decay $B \rightarrow D^{*+} D^{*-}$, which is a mode with similar “ \mathcal{CP} reach” to the famous ψK final state,⁹ requires knowledge of the D meson decay constant, f_D .

To see why there have been measurements of the D_s^+ decay constant, f_{D_s} , and not of f_D or f_B , consider the decay rate for the weak annihilation of a $Q\bar{q}$ pseudoscalar meson, M , into $\ell\nu$.

$$\Gamma(M^+ \rightarrow \ell^+ \nu) = \frac{1}{8\pi} G_F^2 f_M^2 m_\ell^2 M_M \left(1 - \frac{m_\ell^2}{M_M^2}\right)^2 |V_{Qq}|^2 \quad (2)$$

where M_M and m_ℓ are the masses of the meson and lepton, respectively, f_M is the pseudoscalar decay constant, and V_{Qq} is the relevant CKM matrix element. Helicity suppression is evident in the factor of m_ℓ^2 . The B^+ annihilation rates are predicted to be small (with a branching fraction of $\sim 10^{-5}$ for the least helicity suppressed channel $B^+ \rightarrow \tau^+ \nu$) because the relevant CKM matrix element is V_{ub} . The charm annihilation rates are not small but the D_s^+ rates are Cabibbo favored over the D^+ (i.e., by about $|V_{cs}/V_{cd}|^2$) making the D_s^+ leptonic decay the best bet experimentally.

Last year CLEO published¹⁰ a measurement of $\Gamma(D_s^+ \rightarrow \mu^+ \nu)/\Gamma(D_s^+ \rightarrow \phi\pi^+)$. The basic technique involved using the $D_s^{*+} \rightarrow D_s^+ \gamma$ decay chain and the missing

momentum and energy in an event to calculate the neutrino's momentum. A key point to this analysis is that the $\mu\nu$ channel dominates over the $e\nu$ channel because of helicity suppression, but the backgrounds are essentially independent of lepton flavor. Hence, the analysis is performed for both electrons and muons, and whatever remains in the electron analysis is directly subtracted from the $\mu\nu$ sample. The signal is then seen as a peak in the mass difference plot. The results for the updated measurement are shown in Fig. 10. The primary differences

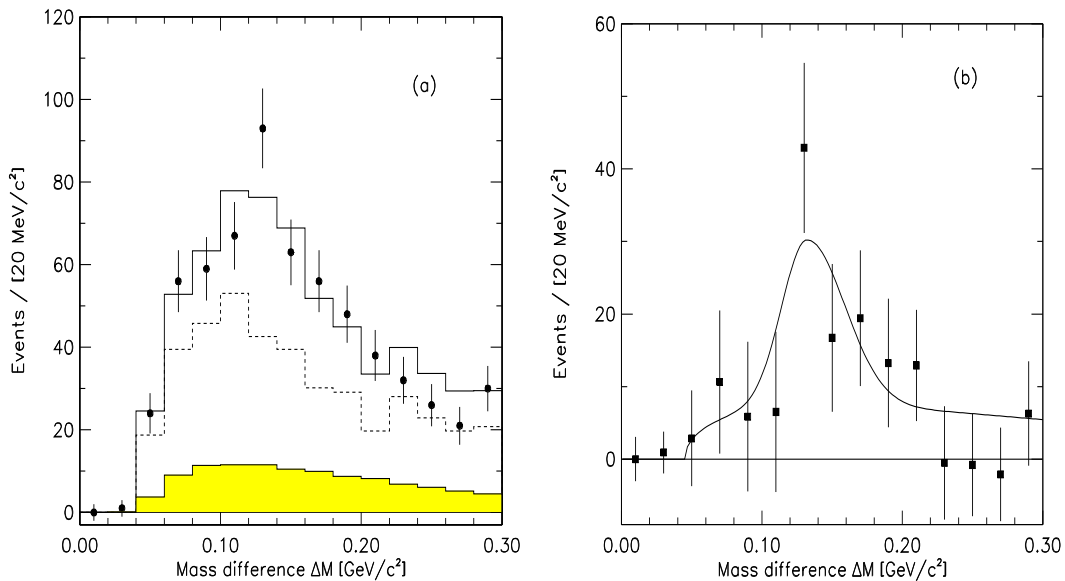


Figure 10: The $\Delta M \equiv M(D_s^+ \gamma) - M(D_s^+)$ distributions in the $D_s^+ \rightarrow \mu^+ \nu$ analysis. Figure (a) includes the muon data (solid points), the electron data (dashed histogram) and excess muon fakes over lepton fakes (shaded histogram). The solid histogram is the result of a fit. Figure (b) shows the distribution after electron and fake subtraction and the resultant fit.

between this update and the published result are the addition of almost 50% more data and much improved measurements of the probability that a hadron is misidentified as a lepton (i.e., the lepton fake rates).

The result is $\Gamma(D_s^+ \rightarrow \mu^+ \nu) / \Gamma(D_s^+ \rightarrow \phi \pi^+) = 0.184 \pm 0.038 \pm 0.038$. Using Eq. (2) along with $\mathcal{B}(D_s^+ \rightarrow \phi \pi^+) = (3.5 \pm 0.4)\%$ and $\tau_{D_s} = (4.67 \pm 0.17) \times 10^{-13} \text{ s}$ (from Ref. 11) gives $f_{D_s} = 284 \pm 30 \pm 30 \pm 16 \text{ MeV}$. The hope is that f_{D_s} can be utilized to calibrate the various theoretical techniques being used to calculate f_B and f_D . A comparison of this result with the theoretical predictions is given in the next section.

3.2.3 A Detour into B Physics: f_{D_s} from $B \rightarrow D_s^{(*)+} \bar{D}^{(*)}$ Decays

In the dominant process leading to two-body decays of the type[‡] $B \rightarrow D_s^{(*)+} \bar{D}^{(*)}$, shown in Fig. 11, the $D_s^{(*)+}$ is produced from the fragmentation of the W^+ .

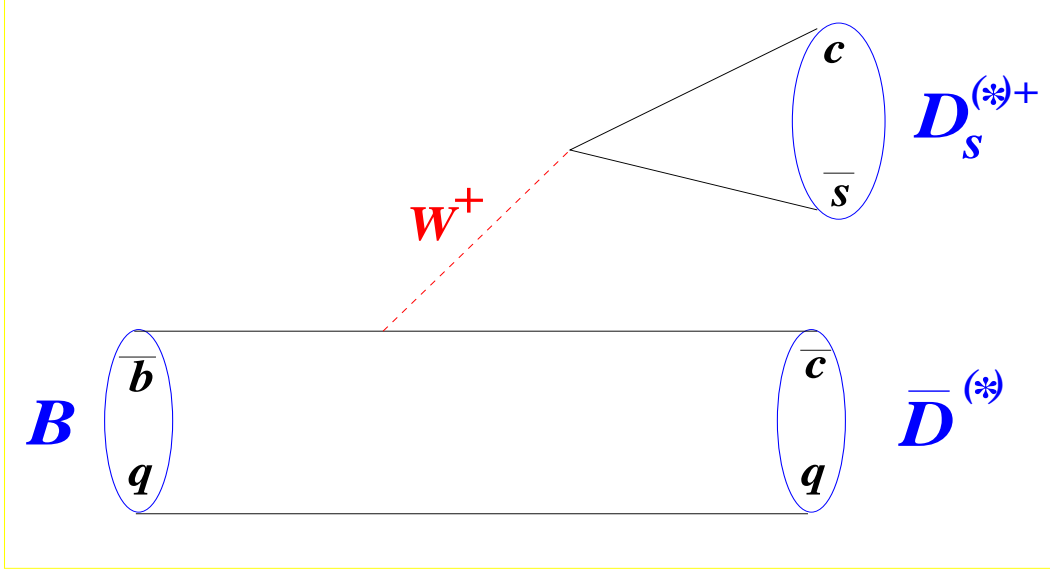


Figure 11: The spectator diagram for $B \rightarrow D_s^{(*)+} \bar{D}^{(*)}$ decay.

Assuming that the decay products of the W^+ do not interact with the final states formed at the $b \rightarrow c$ vertex (in analogy to semileptonic decays), then the amplitude for these decays can be “factorized” into a product of hadronic currents. The branching fraction for $B \rightarrow D_s^+ \bar{D}$ decays, for example, is then given by:

$$\mathcal{B}(B \rightarrow D_s^+ \bar{D}) = K G_F^2 a_1^2 |V_{cb} V_{cs}^*|^2 f_{D_s}^2 F^2(q^2 = m_{D_s}^2) \tau_B$$

where K is a kinematic factor, and the form factor, F , which is a measure of the probability that the \bar{c} and q quarks will bind to form a meson, is a function of q^2 ($= \text{mass}^2$ of the virtual W). The factorization parameter a_1 , which is essentially a QCD correction factor, is the relevant one for external spectator decays like Fig. 11 and can, in principle, be extracted from the measured $B \rightarrow \bar{D} \pi$ branching fractions.

[‡]In $B \rightarrow D_s^{(*)+} \bar{D}^{(*)}$, \bar{D} is a generic representation of the $\bar{c}q$ mesons, the D^- and \bar{D}^0 , while the symbol $(*)$ implies that the branching fraction for both the nonexcited and excited states of the meson were separately measured.

The value of f_{D_s} measured from $D_s^+ \rightarrow \mu^+ \nu$ decays could be used to test the factorization hypothesis in hadronic B decays. Conversely, factorization can be assumed and the measured nonleptonic rates used to extract f_{D_s} , as will be done here. The $B^+ \rightarrow D_s^{(*)+} \bar{D}^{(*)0}$ beam-constrained mass plots from CLEO¹² are shown in Fig. 12. The four B^0 modes are also measured and the “average” branching fractions[§] are found to be:

$$\begin{aligned} \mathcal{B}(B \rightarrow D_s^+ \bar{D}) &= (1.10 \pm 0.17 \pm 0.28 \pm 0.13)\% \\ \mathcal{B}(B \rightarrow D_s^{*+} \bar{D}) &= (0.89 \pm 0.21 \pm 0.20 \pm 0.10)\% \\ \mathcal{B}(B \rightarrow D_s^+ \bar{D}^*) &= (1.12 \pm 0.21 \pm 0.26 \pm 0.13)\% \\ \mathcal{B}(B \rightarrow D_s^{*+} \bar{D}^*) &= (2.41 \pm 0.45 \pm 0.51 \pm 0.29)\% \end{aligned}$$

The D_s^+ decay constant can be extracted from these branching fractions through the use of ratios in which many of the experimental and theoretical errors cancel. Experimental systematic errors are reduced by using CLEO numbers for both the numerator and denominator. The ratio

$$\frac{\Gamma(B \rightarrow \bar{D}^* D_s^+)}{d\Gamma(B \rightarrow \bar{D}^* e^+ \nu_e)/dq^2|_{q^2=m_{D_s}^2}} = 6\pi^2 a_1^2 \delta f_{D_s}^2 |V_{cs}|^2$$

(δ is calculable) has the advantage that the uncertainty in the form factor cancels although a_1 is still present. Conversely, comparing the hadronic rates where the W^+ decays to $u\bar{d}$ as opposed to $c\bar{s}$ gives, for example,

$$\frac{\Gamma(B \rightarrow \bar{D} D_s^+)}{\Gamma(B^0 \rightarrow D^- \pi^+)} = K \frac{f_{D_s}^2 |V_{cs}|^2 F(q^2 = m_{D_s}^2)^2}{f_\pi^2 |V_{ud}|^2 F(q^2 = m_\pi^2)^2}$$

where K is a calculable kinematic factor. The QCD correction factor a_1 cancels (there is some debate on this as discussed in Ref. 12) but model dependence is introduced through the parameterization of the form factor, F , since it is sampled at a different q^2 in the numerator and denominator.

The CLEO results are given in Table 2 along with the theoretical predictions. Both the experimental and theoretical uncertainties need to be reduced before a meaningful comparison can be done. It should be noted, however, that the

[§]That is, $\mathcal{B}(B \rightarrow D_s^{(*)+} \bar{D}^{(*)})$ is the average of the $B^0 \rightarrow D_s^{(*)+} D^{(*)-}$ and $B^+ \rightarrow D_s^{(*)+} D^{(*)0}$ branching fractions. See Ref. 12 for a discussion and justification of this.

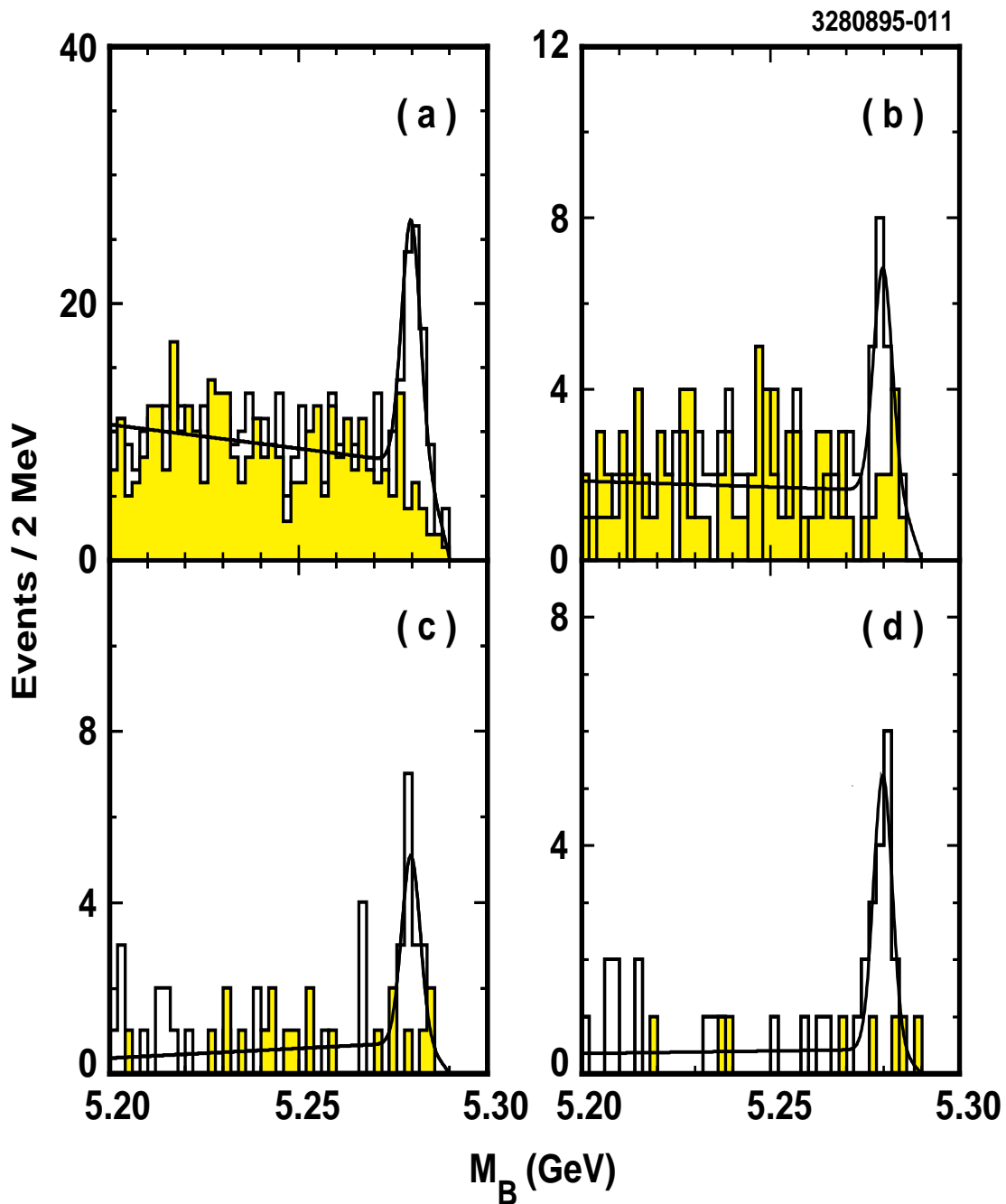


Figure 12: The beam-constrained mass spectra for the B^+ decay modes: (a) $D_s^+ \bar{D}^0$, (b) $D_s^{*+} \bar{D}^0$, (c) $D_s^+ \bar{D}^{*0}$, and (d) $D_s^{*+} \bar{D}^{*0}$. The solid histogram is the data within the ΔE signal window ($|\Delta E| < 25$ MeV) while the filled histogram is the data in ΔE sidebands. The curves are the results of fits where the fitting function consists of a Gaussian to describe the signal and a background function which is linear for $M_B < 5.282$ GeV and parabolic, with a kinematic cutoff, for larger values of M_B .

CLEO II Results	f_{D_s} (MeV)
$D_s^+ \rightarrow \mu^+ \nu_\mu$	$284 \pm 30 \pm 30$
$\Gamma(B \rightarrow D_s^{(*)+} \bar{D}^*) / d\Gamma(B \rightarrow \bar{D}^* e^+ \nu_e) / dq^2 _{q^2=m_{D_s^{(*)}^2}^2}$	$281 \pm 22 \pm 32$
$\sum \Gamma(B \rightarrow D_s^{(*)+} \bar{D}^{(*)}) / \sum \Gamma(B^0 \rightarrow \pi^+ / \rho^+ D^{(*)-})$	$288 \pm 13 \pm 38$
Theoretical Predictions	f_{D_s} (MeV)
Lattice QCD ¹³	235 ± 15
QCD Sum Rules ¹³	260 ± 50
Quark Models ¹⁴	$\sim 290 \pm 20$

Table 2: Determinations of f_{D_s} . A $\mathcal{B}(D_s^+ \rightarrow \phi\pi^+) = (3.5 \pm 0.4)\%$ is common to all experimental results and its uncertainty is not included in the systematic error. A value of $a_1 = 1.07 \pm 0.04 \pm 0.06$ was taken from the CLEO paper¹⁵ on hadronic B decays to final states not including the D_s^+ .

theoretical uncertainties in ratios like f_{D_s}/f_D are generally considered to be under better control and, therefore, a reasonably precise value for f_D could be obtained from a measurement of f_{D_s} .

3.2.4 Semileptonic D_s^+ Decays

Semileptonic decays are particularly simple to treat theoretically because there is only the one diagram and there are no final state interactions.¹⁶ In b quark physics, a precise value for V_{cb} can be arrived at through measurements of $B \rightarrow D^* \ell \nu$ decays and the inclusive lepton momentum spectrum. This is possible because of theoretical advances in understanding the form factors in such heavy-to-heavy (i.e., $b \rightarrow c$) transitions. However, such techniques are not applicable in heavy-to-light transitions like $b \rightarrow u$, thereby complicating the extraction of V_{ub} . Charmed semileptonic decays could be the key to this problem because the CKM matrix elements, V_{cs} and V_{cd} , are known, allowing the heavy-to-light form factors to be probed experimentally. It was perhaps somewhat surprising, given the initial assumptions about the simplicity of semileptonic decays, that the original calculations of $\Gamma(D \rightarrow \bar{K}^* \ell \nu) / \Gamma(D \rightarrow \bar{K} \ell \nu)$ were about a factor of two higher than the experimental value of 0.56 ± 0.05 . Some postdictions do a better job, but it would be very interesting to measure this same vector-to-pseudoscalar ratio for the D_s^+ ,

the “other” charmed meson system.

CLEO has published results on $D_s^+ \rightarrow \phi \ell \nu$ decays.¹⁷ The CLEO II detector is well suited for observing $D_s^+ \rightarrow \eta \ell \nu$ decays because of the power of the CsI calorimeter in reconstructing the two photons from the $\eta \rightarrow \gamma \gamma$ decay chain. The η' is reconstructed through its decay to $\eta \pi^+ \pi^-$. The analysis uses both electrons and muons, although the muon results are corrected for phase space and the final results are then given as semielectronic branching fractions. There are sufficient statistics in the $\phi \ell \nu$ and $\eta \ell \nu$ samples to also perform the analysis by using the $D_s^{*+} \rightarrow D_s^+ \gamma$ mode (the so-called “tagged” analysis). This requirement reduces the backgrounds and allows for the minimum electron momentum to be lowered to 0.7 GeV from the 1 GeV requirement used in the “untagged” analysis. There is actually little correlation between the tagged and untagged results, and they are combined in the $\eta \ell \nu$ case. The mass plots for the untagged analysis are shown in Fig. 13. The results are given in Table 3. Many of the systematic errors cancel in the ratios.

$\Gamma(D_s^+ \rightarrow \eta e^+ \nu) / \Gamma(D_s^+ \rightarrow \phi e^+ \nu)$	$1.24 \pm 0.12 \pm 0.15$
$\Gamma(D_s^+ \rightarrow \eta' e^+ \nu) / \Gamma(D_s^+ \rightarrow \phi e^+ \nu)$	$0.43 \pm 0.11 \pm 0.07$
$\Gamma(D_s^+ \rightarrow \eta' e^+ \nu) / \Gamma(D_s^+ \rightarrow \eta e^+ \nu)$	$0.35 \pm 0.09 \pm 0.07$
$\Gamma(D_s^+ \rightarrow \phi e^+ \nu) / \Gamma(D_s^+ \rightarrow (\eta + \eta') e^+ \nu)$	$0.60 \pm 0.06 \pm 0.06$

Table 3: Summary of measurements for $D_s^+ \rightarrow X e^+ \nu$.

The vector-to-pseudoscalar ratio of $0.60 \pm 0.06 \pm 0.06$ for the D_s^+ agrees nicely with the value for the D meson and with the theoretical predictions. There is some non-negligible dependence in the calculations on the value of the $\eta - \eta'$ mixing angle. The $\Gamma(D_s^+ \rightarrow \eta' e^+ \nu) / \Gamma(D_s^+ \rightarrow \eta e^+ \nu)$ ratio is also interesting since it is predicted to be equal to $\Gamma(D_s^+ \rightarrow \eta' \rho^+) / \Gamma(D_s^+ \rightarrow \eta \rho^+)$ from factorization.¹⁸ However, this ratio of hadronic rates is found by CLEO¹⁹ to be 1.20 ± 0.35 , not in very good agreement with the factorization expectation.

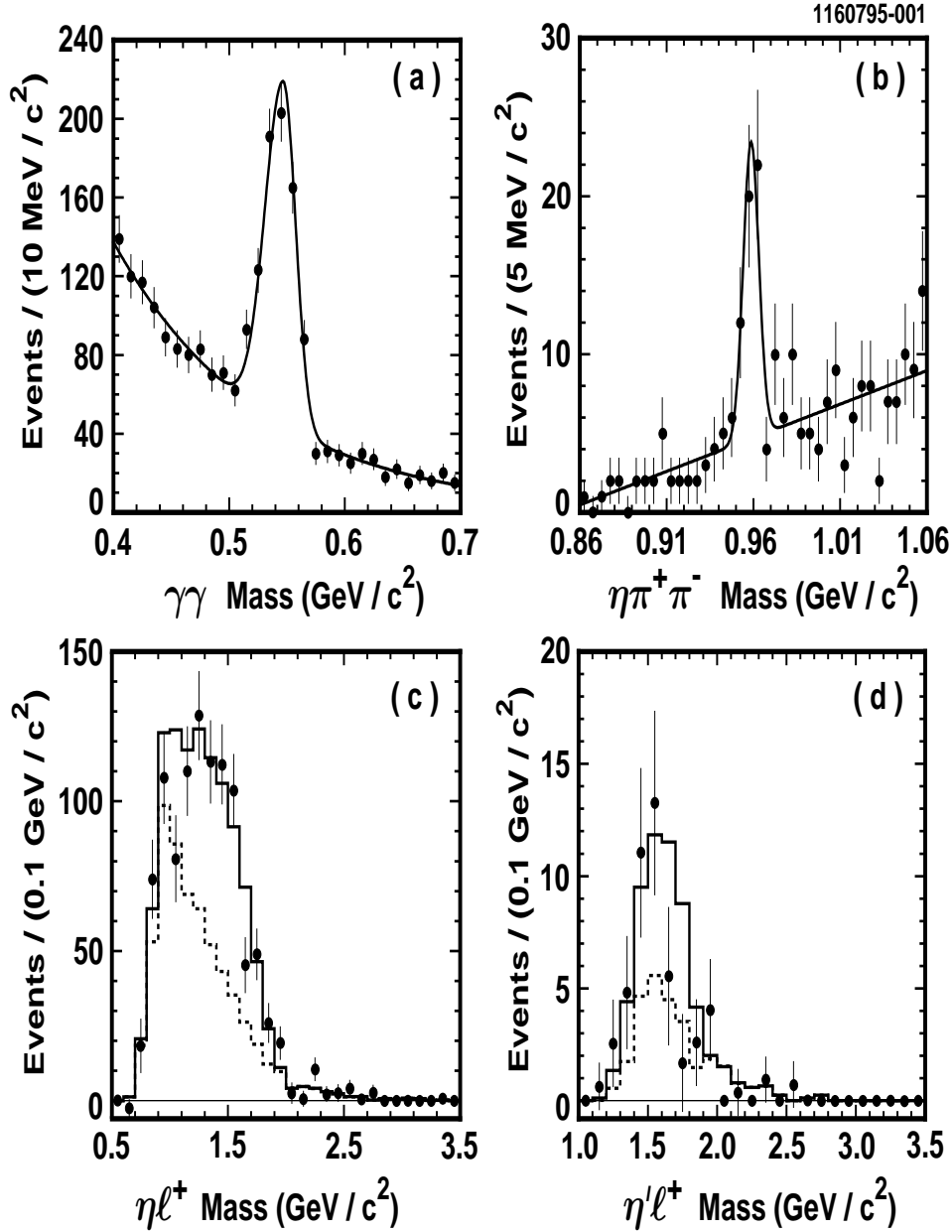


Figure 13: Invariant mass plots for the non- D_s^{*+} tagged $D_s^+ \rightarrow \eta\ell\nu$ and $D_s^+ \rightarrow \eta'\ell\nu$ analysis. The η and η' signals are shown in (a) and (b), respectively. The solid curves are the fits to each spectrum. The $\eta\ell^+$ and $\eta'\ell^+$ mass spectra are shown in (c) and (d), respectively. The solid histogram shows the simulated signal plus the predicted background while the dotted histogram is the predicted background alone.

4 Bottom Mesons

The basic B meson decay diagrams are given in Fig. 15. The spectator diagram dominates the rate although the color suppressed (or, internal W decay) diagram is a significant player as evidenced by the large $B \rightarrow \psi^{(\prime)} X$ branching fractions.²⁰ Neither the annihilation nor the W -exchange process has been observed, and their total rates are expected to be small. CLEO observed the inclusive branching fraction for the radiative penguin to be around 2×10^{-4} while there is no unambiguous evidence for gluonic penguin decays (see Sec. 4.2.1). There is some question as to whether even the dominant decay processes are understood, as will be discussed in the next session. The following sections will be concerned with rare decays — in particular, a search for gluonic penguin decays and the first observation of an exclusive semileptonic $b \rightarrow u$ decay channel.

4.1 $b \rightarrow c$ Decays and the Charm Count

Assuming that the diagram of Fig. 14 dominates[¶] and that the $b \rightarrow u$ contribution

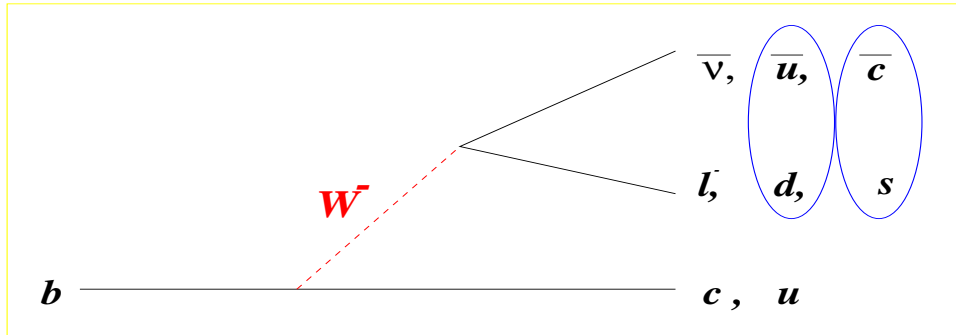


Figure 14: The dominant b quark decay diagram.

is negligible, then the total B meson decay rate, Γ , is given by:

$$\Gamma = \Gamma(b \rightarrow c\ell^-\bar{\nu}) + \Gamma(b \rightarrow c\bar{u}d) + \Gamma(b \rightarrow c\bar{c}s).$$

In terms of branching fractions, this becomes:

$$\mathcal{B}(B \rightarrow X\ell\nu) = 1 - \mathcal{B}(b \rightarrow c\bar{u}d) - \mathcal{B}(b \rightarrow c\bar{c}s). \quad (3)$$

[¶]The Cabibbo-suppressed channels like $c\bar{u}s$ are implicitly included here as are the internal W decay channels.

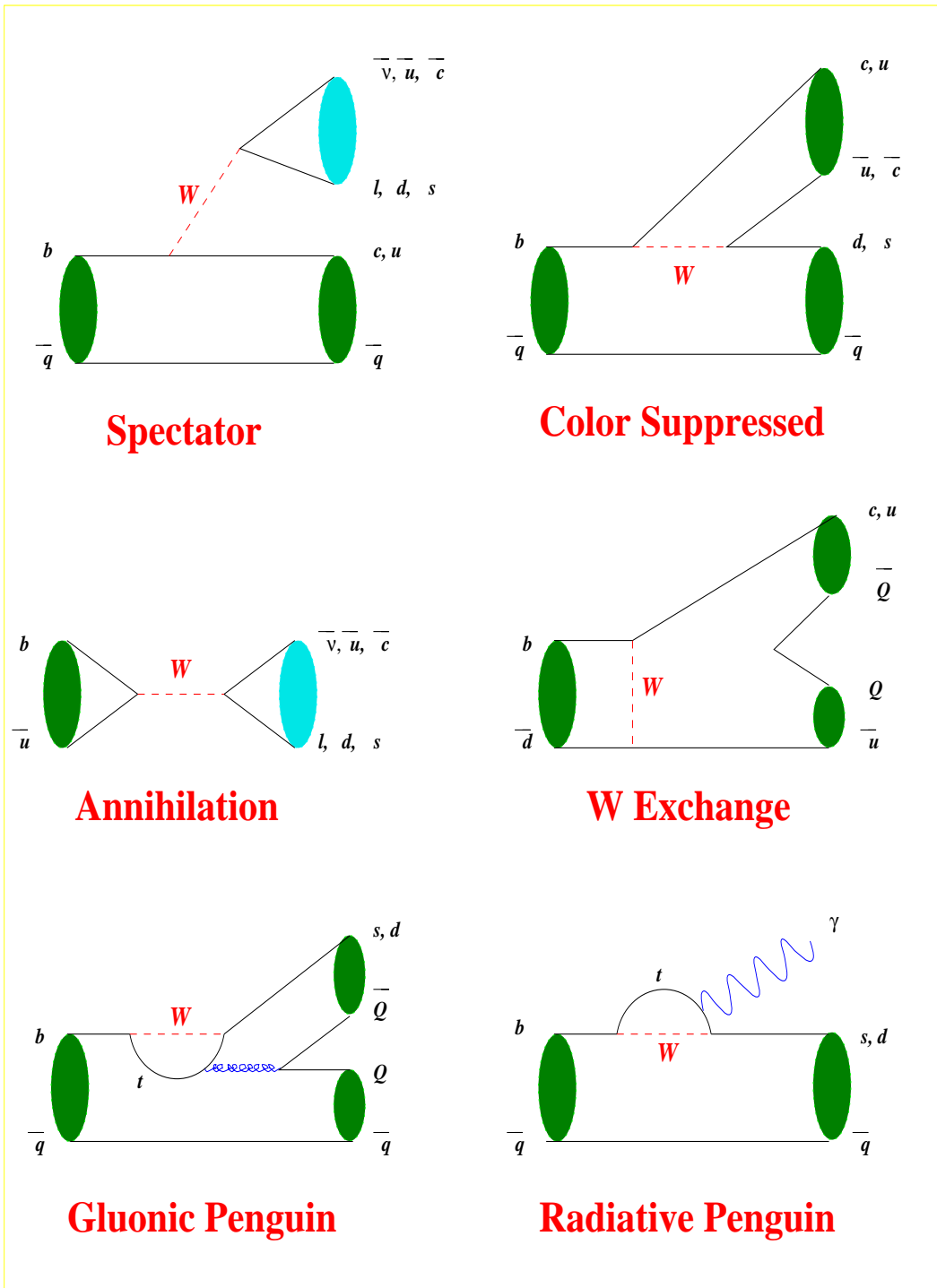


Figure 15: B meson decay diagrams.

If all lepton and quark masses were small relative to m_B , and there were no complications due to strong interactions, then $\mathcal{B}(B \rightarrow X e^+ \nu) \equiv \mathcal{B}_e$ would be 1/9. Phase space corrections due to the large τ^+ lepton and charm quark masses raises \mathcal{B}_e to about 17%. Bigi and collaborators claimed²¹ that, even including all QCD corrections, the lower limit on the semielecronic B branching fraction is 12.5%. Yet measurements from CLEO, ARGUS, and LEP consistently find \mathcal{B}_e to be less than 11%, hence the moniker “baffling” for this branching fraction.

The measurements have predominantly come from fitting the momentum spectrum of leptons from B decay. Part of the difficulty in extracting \mathcal{B}_e from the inclusive lepton momentum spectrum is that leptons in B meson decays come not only from the primary $b \rightarrow c \ell \nu$ decay mechanism but also from the subsequent semileptonic decay of the charm quark. Thus a large model dependence is introduced when trying to extract \mathcal{B}_e since fitting the spectrum requires a functional form for both components.

A way around this difficulty is to tag the flavor of the decaying b quark. In the B meson rest frame (essentially the lab frame for CLEO), the leptons from the secondary charm quark decay are generally “soft”, with only about 3% having momentum greater than 1.4 GeV. In $\Upsilon(4S)$ decays there are no other particles produced along with the B and \bar{B} mesons. Therefore, using a high momentum lepton to tag the charge of one of them essentially tags the charge of both (with a calculable correction due to mixing in $B^0 \bar{B}^0$ events). This is illustrated in Fig. 16. In this example, the ℓ^+ tag indicates that a \bar{b} decayed semileptonically. If there

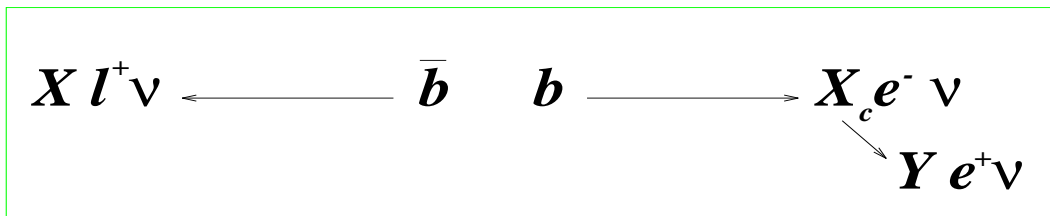


Figure 16: Charge correlations in the lepton tagged measurement of the semielecronic B branching fraction.

is a second lepton in the event, then this lepton’s charge distinguishes whether it came from the decay of the b quark or from the semileptonic decay of the charmed hadron produced in the weak $b \rightarrow c$ decay.

This technique was first proposed by ARGUS, and CLEO added a momentum-dependent cut on the angle between the tag lepton and the second lepton to

eliminate events where the two leptons come from the same B . Both electrons and muons are used by CLEO as tags. Only electrons are used as the second lepton since the detector is efficient down to electron momenta of 600 MeV whereas the muon fake rates get large for muons of momentum below 1.4 GeV. Using this technique allows for the separation of the primary and cascade lepton momentum spectra, as shown in Fig. 17. The $B \rightarrow Xe^+\nu$ branching fraction is found to be $(10.49 \pm 0.17 \pm 0.43)\%$. Some small model dependence comes in when accounting for the undetected fraction of the spectrum below 600 MeV. This was estimated to comprise $(6.1 \pm 0.5)\%$ of the total.

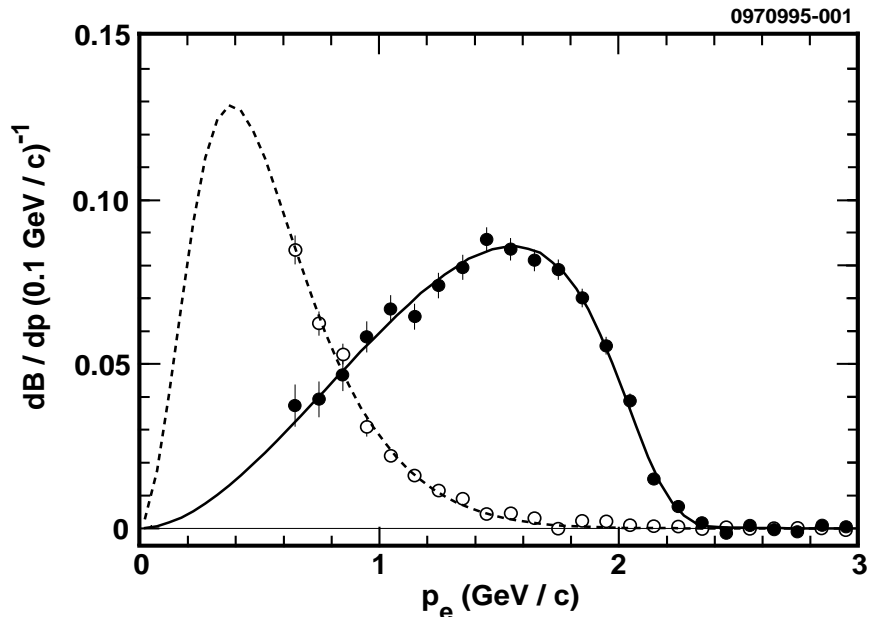


Figure 17: The spectra of electrons from $B \rightarrow Xe\nu$ (filled circles) and $b \rightarrow c \rightarrow Ye\nu$ (open circles) after continuum and fake subtraction, and the mixing correction. The curve is an example of one of the fits used to estimate the uncertainty in the extrapolation from 600 MeV to the origin.

This model-independent measurement strongly supports the conclusion that the semielectronic B branching fraction is significantly below 12.5%. It is clear from Eq. (3) that for $\mathcal{B}(B \rightarrow X\ell\nu)$ to go down, $\mathcal{B}(b \rightarrow c\bar{u}d) + \mathcal{B}(b \rightarrow c\bar{c}s)$ must go up. Recent calculations²² have shown that higher order perturbative corrections lower the value of \mathcal{B}_e considerably but at the price of simultaneously raising the

contribution from $\mathcal{B}(b \rightarrow c\bar{c}s)$ decays. Since this final state contains two charm quarks, this prediction has the experimentally observable result of raising n_c , the number of charm quarks per B decay, from the value of around 1.15 associated with the larger predicted \mathcal{B}_e to > 1.3 . The number of charm quarks per B decay can be calculated using the measured inclusive branching fractions. Naively this is given by:

$$\begin{aligned}
n_c = & \mathcal{B}(B \rightarrow D^0 X) + \mathcal{B}(B \rightarrow D^+ X) + \mathcal{B}(B \rightarrow D_s X) \\
& + \mathcal{B}(B \rightarrow \Lambda_c X) + \mathcal{B}(B \rightarrow \Xi_c^+ X) + \mathcal{B}(B \rightarrow \Xi_c^0 X) \\
& + 2\mathcal{B}(B \rightarrow \psi X) + 2\mathcal{B}(B \rightarrow \psi' X) \\
& + 2\mathcal{B}(B \rightarrow \chi_{c1} X) + 2\mathcal{B}(B \rightarrow \chi_{c2} X) + 2\mathcal{B}(B \rightarrow \eta_c X) \quad (4)
\end{aligned}$$

where some assumptions must be made about how baryons and D_s^+ mesons are produced in B decay. CLEO has released new, more precise values for all of these branching fractions in the last year except for the D^0 and D^+ final states where the new measurements should be available in early 1996. The experimental value of n_c is around the 1.15 with an uncertainty of about 0.05. The dominant uncertainties in many of these branching fractions are systematic, some of which are correlated, so it is difficult to get a precise value for the uncertainty in n_c . Even given this, however, the data do not support an enhanced $\mathcal{B}(b \rightarrow c\bar{c}s)$ component so \mathcal{B}_e will remain “baffling” for a while yet.

4.2 Rare Hadronic B Decays

CLEO has investigated a slew of rare hadronic B decay channels including the $\pi\pi$, $K\pi$, and KK final states (with both charged and neutral kaons and pions) as well as the $\pi\rho$, $K\rho$, $K^*\pi$, $K\phi$, $K^*\phi$, and $\phi\phi$ final states.²³ There is still no significant signal in any particular channel although the upper limits on the branching fractions for some, e.g. $\pi^+\pi^-$, $\pi^+\pi^0$, and $\pi^+\rho^-$, are encroaching on the theoretical predictions. The beam-constrained mass plots for the $\pi\pi$, $K\pi$, and KK channels are shown in Fig. 18.

The combined $\pi^+\pi^-$ and $K^+\pi^-$ signal is now > 4 standard deviations from 0 although the K/π separation of $\sim 1.8\sigma$ is still not enough to resolve the two states with the present statistics. This is illustrated in Fig. 19 which shows the results of the maximum likelihood fit to the two charged track final state.

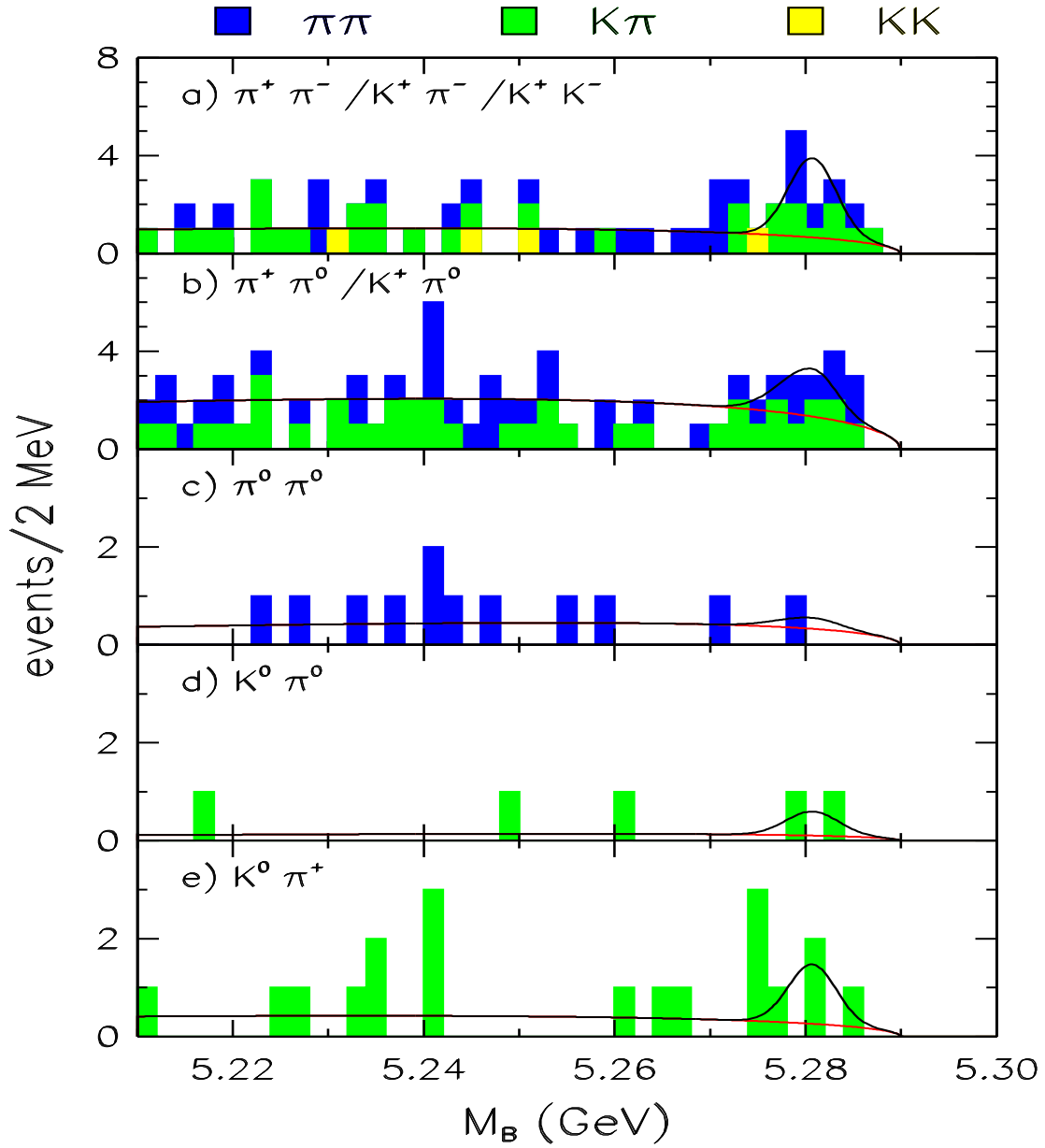


Figure 18: The beam-constrained mass spectra for the $\pi\pi$, $K\pi$, and KK channels. The modes in (a) and (b) are sorted by dE/dx according to the most likely hypothesis.

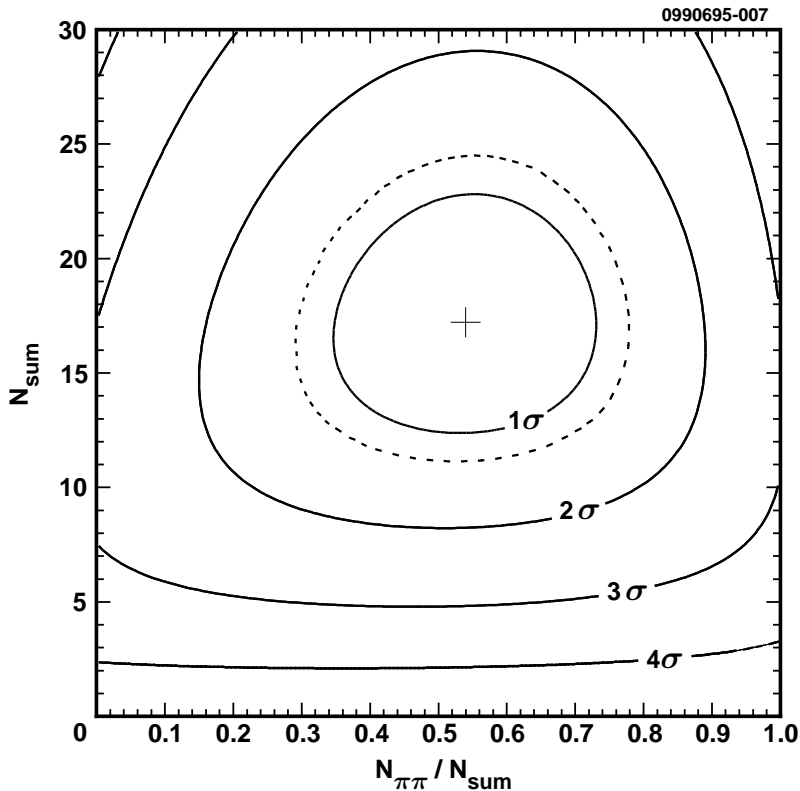


Figure 19: The central value (+) of the likelihood fit to $N_{sum} \equiv N_{\pi\pi} + N_{K\pi}$ and $N_{\pi\pi}/N_{sum}$ for $B^0 \rightarrow \pi^+\pi^-$ and $B^0 \rightarrow K^+\pi^-$. The solid curves are the $n\sigma$ contours and the dotted curve is the 1.28σ contour.

4.2.1 Penguin Pollution and $B \rightarrow X_s \phi$

The $B^0 \rightarrow \pi^+\pi^-$ decay channel is of great interest because it is one of the modes that can be used at an asymmetric “ B Factory” to measure an angle of the unitarity triangle. There is one caveat to this, however, and that is so-called “Penguin Pollution,” which is illustrated in Fig. 20. Only for the top diagram in Fig. 20 can an angle of the unitarity triangle be cleanly extracted from measurements of time-dependent decay asymmetries in $B^0 \rightarrow \pi^+\pi^-$ decays. If the contribution to the rate from the bottom diagram in Fig. 20, the gluonic penguin diagram, is non-negligible, then a more complicated isospin analysis of the full $\pi\pi$ system must be done to get to the desired information on the CKM matrix.²⁴

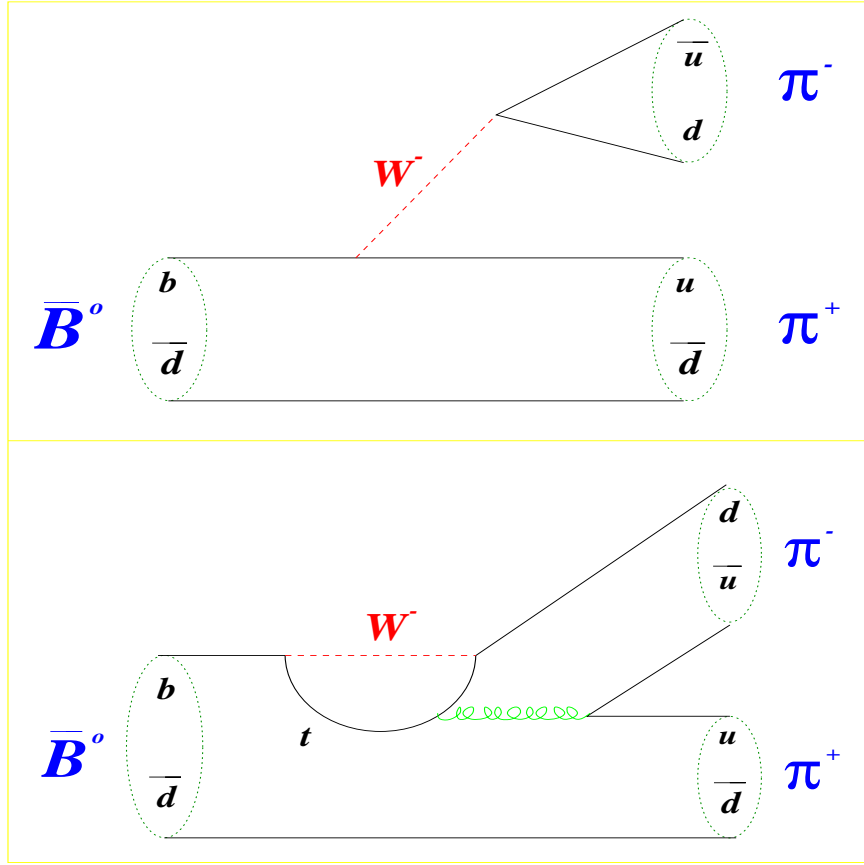


Figure 20: The tree level (top) and gluonic penguin (bottom) diagrams for the $B \rightarrow \pi^+\pi^-$ decay channel.

It is extremely difficult to calculate the relative strength of the gluonic penguin in decays like $B^0 \rightarrow \pi^+\pi^-$, and so it would be desirable to observe a decay which proceeds solely through this mechanism. Assuming that weak annihilation processes producing the $s\bar{s}$ final state (e.g., $b\bar{u} \rightarrow W^- \rightarrow s\bar{u}$ with $s\bar{s}$ popping) are negligible, then $b \rightarrow s\bar{s}s$ decay proceeds through a penguin decay process. The gluonic penguin, illustrated in Fig. 21, is expected to dominate over the electromagnetic penguin so the observation of decays of the form $B \rightarrow X_s\phi$ (where X_s can be one particle or a system of particles with net strangeness 1) would be an unambiguous signature for the gluonic penguin. Theoretical understanding of such rates would lead to some confidence that the contributions of these diagrams to other processes could be reliably calculated.

The upper limits from CLEO on some exclusive $B \rightarrow X_s\phi$ branching fractions are given in Table 4. While these branching fractions indicate that this process is not dominating the rate, there is uncertainty in how the $s\bar{s}s\bar{q}$ final state hadronizes.

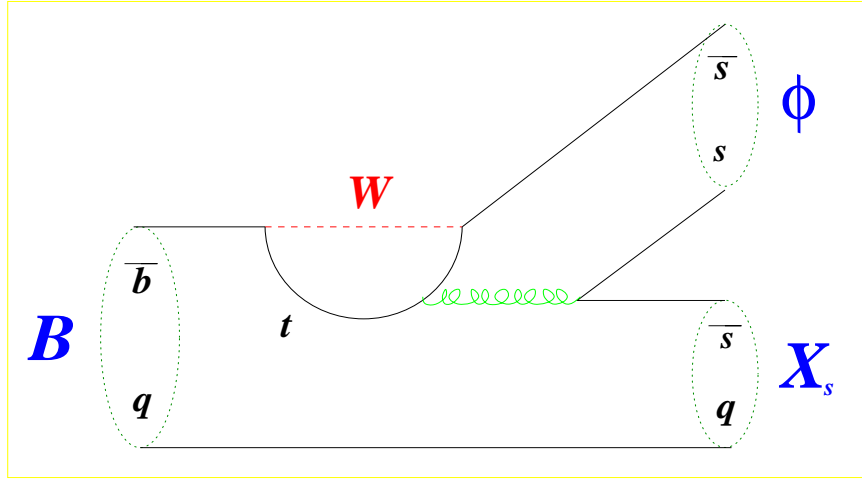


Figure 21: The pure penguin $B \rightarrow X_s \phi$ decay.

This motivates a measurement of the inclusive $b \rightarrow sg \rightarrow s\bar{s}s$ rate since it may be calculable from first principles and should be at least an order of magnitude higher than the rate for any exclusive channel. Some schemes even have very large rates for this, “solving” the baffling semielectronic branching fraction problem without raising n_c (see Sec. 4.1).

Decay Mode	CLEO II Upper Limit
$B^0 \rightarrow K_S^0 \phi$	$< 4.4 \times 10^{-5}$
$B^+ \rightarrow K^+ \phi$	$< 1.2 \times 10^{-5}$
$B^0 \rightarrow K^{*0} \phi$	$< 4.3 \times 10^{-5}$
$B^+ \rightarrow K^{*+} \phi$	$< 7.0 \times 10^{-5}$

Table 4: Upper limits on exclusive $B \rightarrow X_s \phi$ branching fractions.

Two techniques are used to search for $B \rightarrow X_s \phi$. One method involves searching for ϕ mesons from B decay with momenta beyond the endpoint for having originated from the standard tree level B decays. The continuum-subtracted ϕ momentum spectrum is the left-hand plot in Fig. 22. There is no evidence of an excess in the signal region of $0.4 < x < 0.5$ and the 90% confidence level upper limit is found to be $\mathcal{B}(B \rightarrow X_s \phi) < 2.2 \times 10^{-4}$ for $2.0 < p_\phi < 2.6$ GeV. The other technique, the so-called “ B Reconstruction” technique, is a slight variation of the method that was found to be very powerful in the measurement of the inclusive $b \rightarrow s\gamma$ rate.²⁵ The basic idea is to combine a K^+K^- pair which reconstruct to

within ± 20 MeV of the ϕ mass, a kaon (either a K^\pm or a $K_S^0 \rightarrow \pi^+\pi^-$), and zero to four pions (with at most one π^0), and to keep the “best” (i.e., most likely B) combination based on beam-constrained mass, ΔE , particle ID, and K_S^0 or π^0 mass, if they are used. The goal here is not to fully reconstruct these exclusive final states but to reject continuum background which is much less likely than the signal to satisfy these criteria. The results of this analysis are shown in the right-hand plots in Fig. 22 where again there is no evidence for a signal above the continuum. The 90% confidence level upper limit for this technique is found to be $\mathcal{B}(B \rightarrow X_s \phi) < 1.1 \times 10^{-4}$. The two methods are complementary since, even though the first one is not as powerful at suppressing background, it is much less sensitive to the details of how the $s\bar{q}s\bar{s}$ final state hadronizes. It is clear from these measurements that the gluonic penguin rate is not anomalously high although a rate large enough to complicate the extraction of CKM parameters from measurements at an asymmetric B Factory is not ruled out.

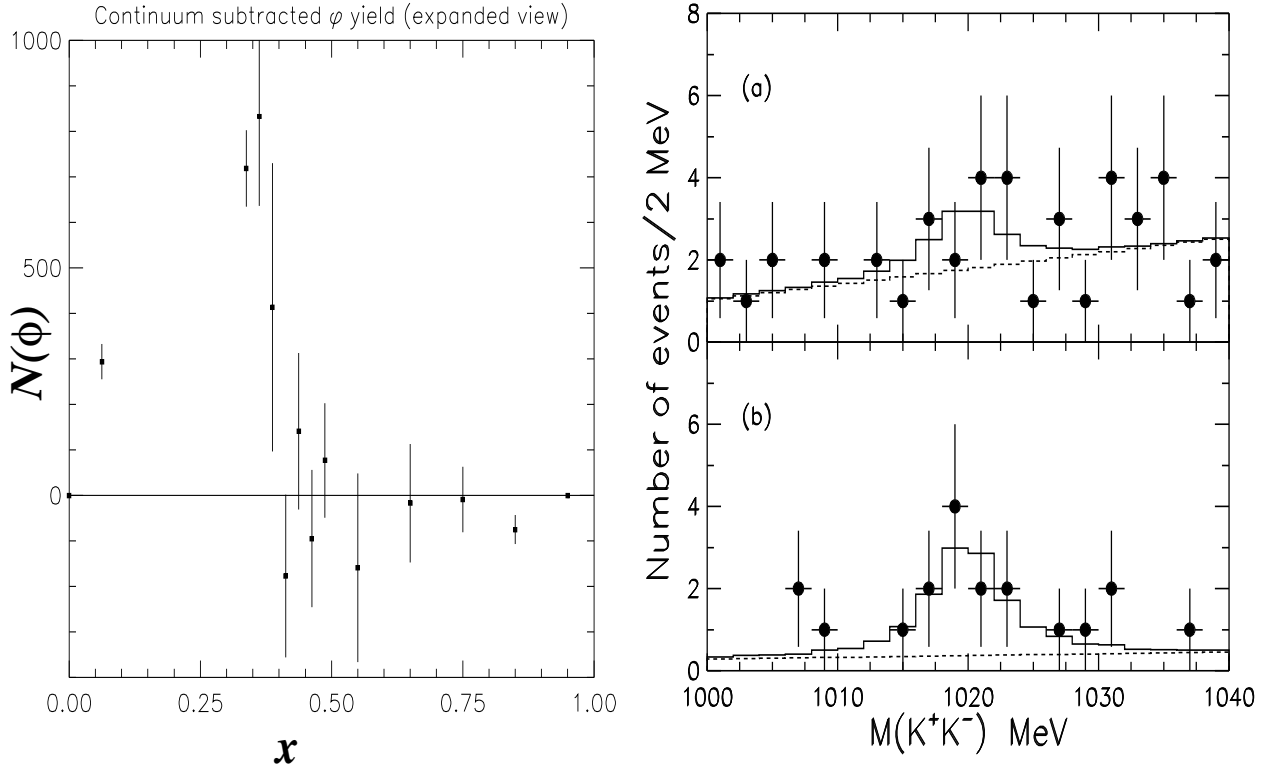


Figure 22: Searches for $B \rightarrow X_s \phi$. The left-hand plot is the continuum subtracted ϕ yield as a function of x . The “signal” region is $0.4 < x < 0.5$. The right-hand plots are the K^+K^- invariant mass for the “ B Reconstruction” candidates (defined in the text) for (a) on-resonance data and (b) continuum data.

4.3 “Neutrino Reconstruction” and the Observation of Exclusive Semileptonic $b \rightarrow u\ell\nu$ Decays

The measurement of V_{ub} is perhaps the most important activity in B physics today. ARGUS and CLEO established that $V_{ub} > 0$ by observing leptons with momentum beyond the endpoint for $b \rightarrow c$ transitions.^{26,27} However, there are large theoretical uncertainties as to the fraction of the rate encompassed by these measurements thus complicating the extraction of V_{ub} . The ratio $|V_{ub}/V_{cb}|$ is presently known to be between 0.07 and 0.11, with theoretical uncertainties determining the size of this range. There is some hope that measurements of exclusive semileptonic $b \rightarrow u\ell\nu$ decays could lead to a more precise determination of $|V_{ub}/V_{cb}|$ because the form factors in such heavy-to-light transitions can be measured experimentally using semileptonic charm decays (see Sec. 3.2.4).

The problem in reconstructing an exclusive $b \rightarrow u\ell\nu$ decay is, of course, that the neutrino is not detected. However, the excellent hermiticity of the CLEO II detector (coverage of $\sim 95\%$ and $\sim 98\%$ of 4π for tracks and photons, respectively) allows for the neutrino four-momentum to be “reconstructed” by using the “missing” energy and momentum in an event. Specifically,

$$E_\nu = E_{miss} \equiv 2E_{beam} - \sum_i E_i \quad (\sigma \sim 260 \text{ MeV})$$

$$\vec{p}_\nu = \vec{p}_{miss} \equiv -\sum_i \vec{p}_i \quad (\sigma \sim 110 \text{ MeV})$$

where the index i runs over all charged tracks and showers in the calorimeter not associated with charged tracks. The resolutions given are for events with no K_L^0 mesons or extra neutrinos. For a real neutrino, $M_{miss}^2 = E_{miss}^2 - |\vec{p}_{miss}|^2$ should be consistent with zero. The criterion $(M_{miss}^2/2E_{miss}) < 300 \text{ MeV}$ is used because the resolution in M_{miss}^2 varies roughly like $2E_{miss}\sigma_{E_{miss}}$. The neutrino energy is set to $|\vec{p}_{miss}|$ because of the better momentum resolution.

Further requirements are then imposed on events to suppress background. Only one charged lepton is allowed per event since another charged lepton immediately implies there being another neutrino. Also, the total charge of an event is required to be zero to ensure that a charged track has not been missed. For a candidate event, this “reconstructed” neutrino can then be used to fully reconstruct a B meson, and the standard beam-constrained mass and ΔE variables can be examined.

The method outlined to this point could be used to reconstruct any exclusive semileptonic B decay mode. It is useful to perform the analysis on a $b \rightarrow c\ell\nu$ channel that has been well measured using the standard missing mass techniques as a test of the “neutrino reconstruction” technique itself and as a measure of the systematic error. The results from an analysis of the $B^0 \rightarrow D^{*-}\ell^+\nu$ decay mode are shown in Fig. 23 where there is good agreement between the data and the

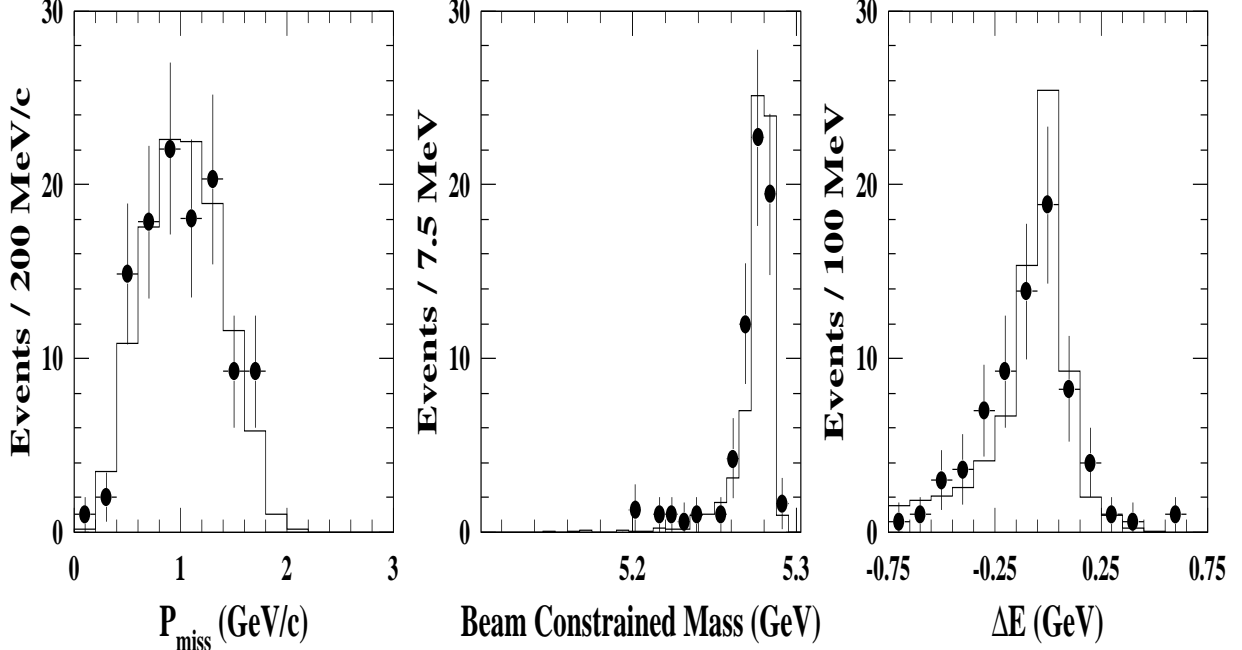


Figure 23: The “Neutrino Reconstruction” distributions in an analysis of the $B^0 \rightarrow D^{*-}\ell^+\nu$ decay chain. The points with error bars are the data and the histograms are from the Monte Carlo simulation.

Monte Carlo for the various kinematic distributions. The neutrino reconstruction result of $\mathcal{B}(B^0 \rightarrow D^{*-}\ell^+\nu) = (4.65 \pm 0.65)\%$ agrees with the CLEO published number²⁸ of $\mathcal{B}(B^0 \rightarrow D^{*-}\ell^+\nu) = (4.49 \pm 0.32 \pm 0.32)\%$.

Five modes are searched for in the $b \rightarrow u$ analysis — the pseudoscalar modes $\pi^-\ell^+\nu$ and $\pi^0\ell^+\nu$, and the vector modes $\rho^-\ell^+\nu$, $\rho^0\ell^+\nu$, and $\omega\ell^+\nu$. Both electrons and muons are used and, to suppress the $b \rightarrow c\ell\nu$ backgrounds, the leptons are required to have momenta greater than 1.5(2) GeV in the pseudoscalar(vector) modes. When extracting the yields, the ΔE - m_B distributions for the five modes are fit simultaneously. This allows for the utilization of the isospin constraints $\Gamma(B^0 \rightarrow \pi^-\ell^+\nu) = 2\Gamma(B^+ \rightarrow \pi^0\ell^+\nu)$ and $\Gamma(B^0 \rightarrow \rho^-\ell^+\nu) = 2\Gamma(B^+ \rightarrow \rho^0\ell^+\nu) \approx 2\Gamma(B^+ \rightarrow \omega\ell^+\nu)$. This method also allows for the feed-across from the vector to

pseudoscalar modes to be handled in a consistent manner.

A further complication in the vector modes are nonresonant $\pi^-\pi^0$, $\pi^-\pi^+$, and $\pi^-\pi^+\pi^0$ contributions, for which neither the rate nor the shape is known. This is dealt with in three different ways: (1) fit for the rates with just a simple cut in $\pi\pi(3\pi)$ mass around the $\rho(\omega)$, (2) fit for the rates after subtracting from the $\pi\pi(3\pi)$ mass in the $\rho(\omega)$ peak regions sideband samples in $\pi\pi(3\pi)$ mass, and (3) include the $\pi\pi(3\pi)$ distributions in the fit where additional assumptions must be made about the shapes of the nonresonant and background components. To illustrate the results from method (2), the beam-constrained mass plots for the ΔE signal region are shown in Fig. 24.

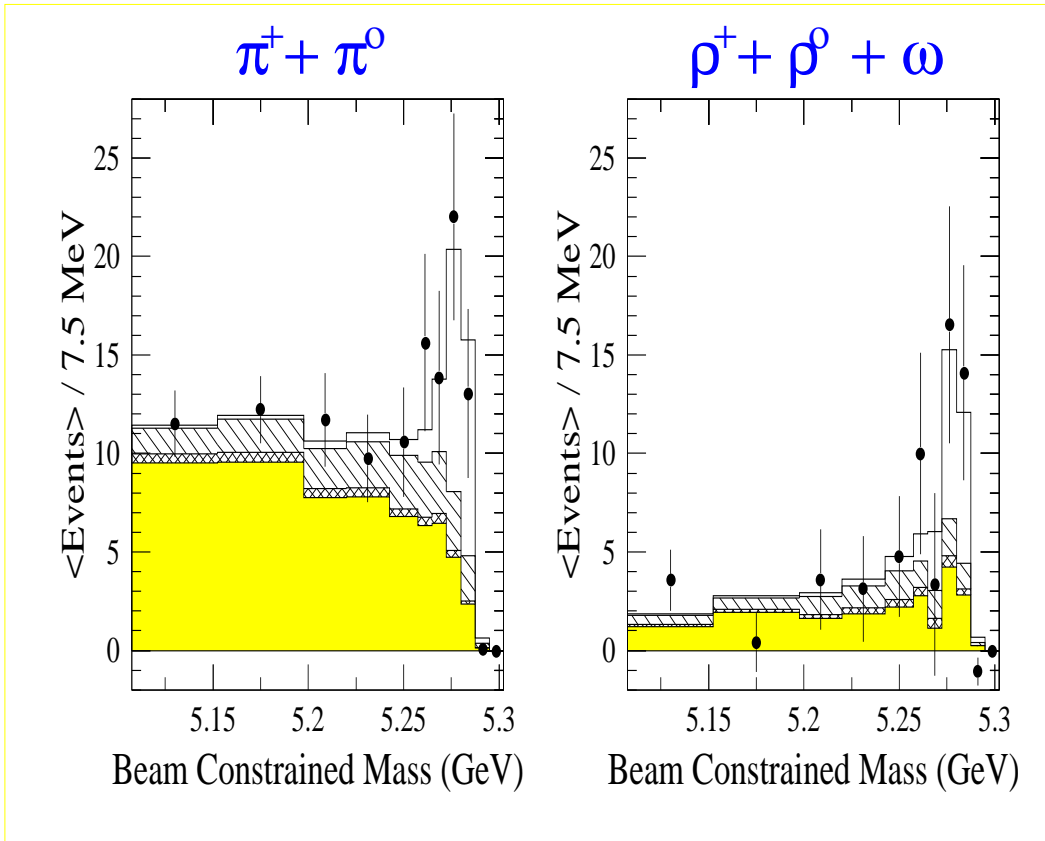


Figure 24: Beam-constrained mass distributions for the combined $\pi^-\ell^+\nu$ and $\pi^-\ell^+\nu$ (left) channels, and the sum of the vector modes (right) for the analysis with $\pi\pi/3\pi$ mass sideband subtractions. The points with error bars are the continuum- and fake-subtracted data. The histograms are the signal (hollow), the contribution from $b \rightarrow c\ell\nu$ (shaded), feed-down from higher mass $b \rightarrow u\ell\nu$ (cross-hatched), and signal mode cross-feed (hatched).

The yields in the vector modes from the different methods are about equal, indicating that there is very little nonresonant contribution to the rate.

Several other distributions were examined to check that these signals are consistent with having come from $b \rightarrow u\ell\nu$ decays. The lepton momentum spectra for the $\Delta E-M_B$ signal region are shown in Fig. 25 where, needless to say, the lepton momentum cuts have been removed in these plots. The lepton momentum

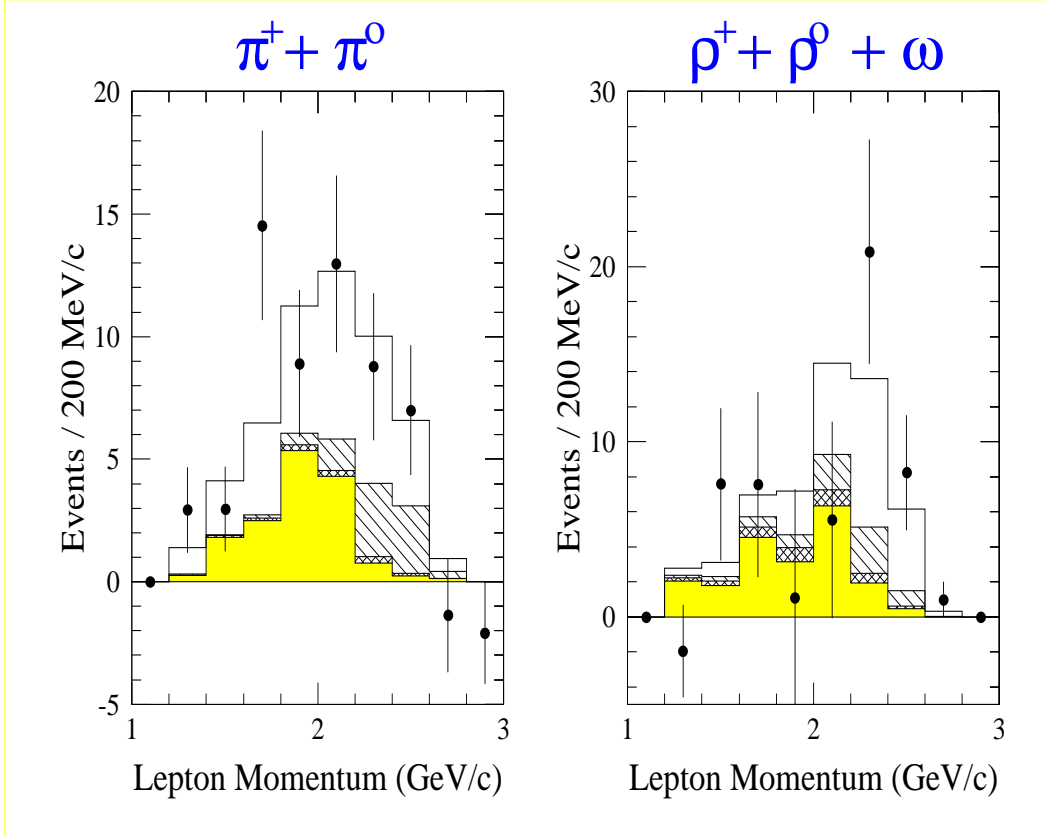


Figure 25: Lepton momentum spectra for $B \rightarrow \pi\ell\nu$ (left) and $B \rightarrow \rho\ell\nu$ (right). The various components have the same meanings as in Fig. 24 (except that here the points are also sideband subtracted) where the normalizations are predictions using the results of the fit to the mass spectra.

spectra are quite “hard,” with many leptons beyond the $b \rightarrow c$ endpoint, indicative of having originated from $b \rightarrow u$ transitions. The exact shapes of the lepton momentum spectra depend on the poorly known $b \rightarrow u$ form factors.

There is form factor independent information in the distribution of the angle defined in Fig. 26. Because of the $V - A$ structure of the weak interaction, the signal in the pseudoscalar case follows a $\sin^2 \theta_{\pi\ell}$ distribution. For the vector

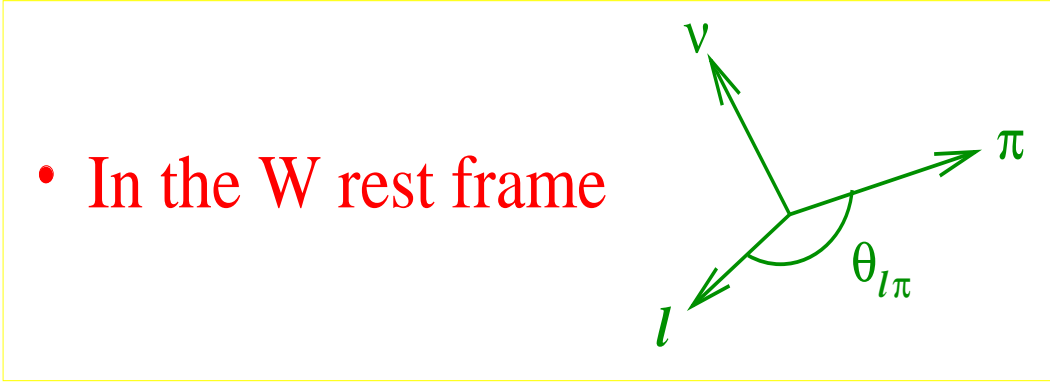


Figure 26: Definition of $\theta_{\pi\ell}$ in $B \rightarrow \pi\ell\nu$ decays. The angle for the vector meson case, $\theta_{\rho\ell}$, follows by replacing the pion with a vector meson.

modes, the details of the angular distributions depend on the form factor but a forward peaking in $\cos\theta_{\rho\ell}$ is expected. The distributions, shown in Fig. 27, are quite consistent with the $b \rightarrow u$ nature of the decays.

The final branching fractions are model dependent because the efficiencies for the various modes depend on the form factors used in the Monte Carlo. Specifically, different form factors concentrate the rate in different regions of q^2 , and the efficiency is a function of q^2 . Results obtained for the WSB and ISGW^{||} models are:^{29,30}

$$\begin{aligned} \mathcal{B}(B^0 \rightarrow \pi^- \ell^+ \nu) &= (1.34 \pm 0.35 \pm 0.28) \times 10^{-4} \quad \text{ISGW} \\ &= (1.63 \pm 0.46 \pm 0.34) \times 10^{-4} \quad \text{WSB} \end{aligned}$$

$$\begin{aligned} \mathcal{B}(B^0 \rightarrow \rho^- \ell^+ \nu) &= (2.28 \pm 0.36 \pm 0.59_{-0.46}^{+0.00}) \times 10^{-4} \quad \text{ISGW} \\ &= (3.88 \pm 0.54 \pm 1.01_{-0.78}^{+0.00}) \times 10^{-4} \quad \text{WSB} \end{aligned}$$

where the third error for the vector mode is the uncertainty due to the non-resonant contribution.

There is some potential to discriminate between models using the ratio of rates. The results are given in Table 5 where the ISGW prediction appears to be inconsistent with the data. More studies of the model dependence need to be performed before a value of V_{ub} can be extracted from this analysis.

^{||}This is the ‘original’ ISGW. Results including the so-called ISGW2 model will be included in the final analysis.

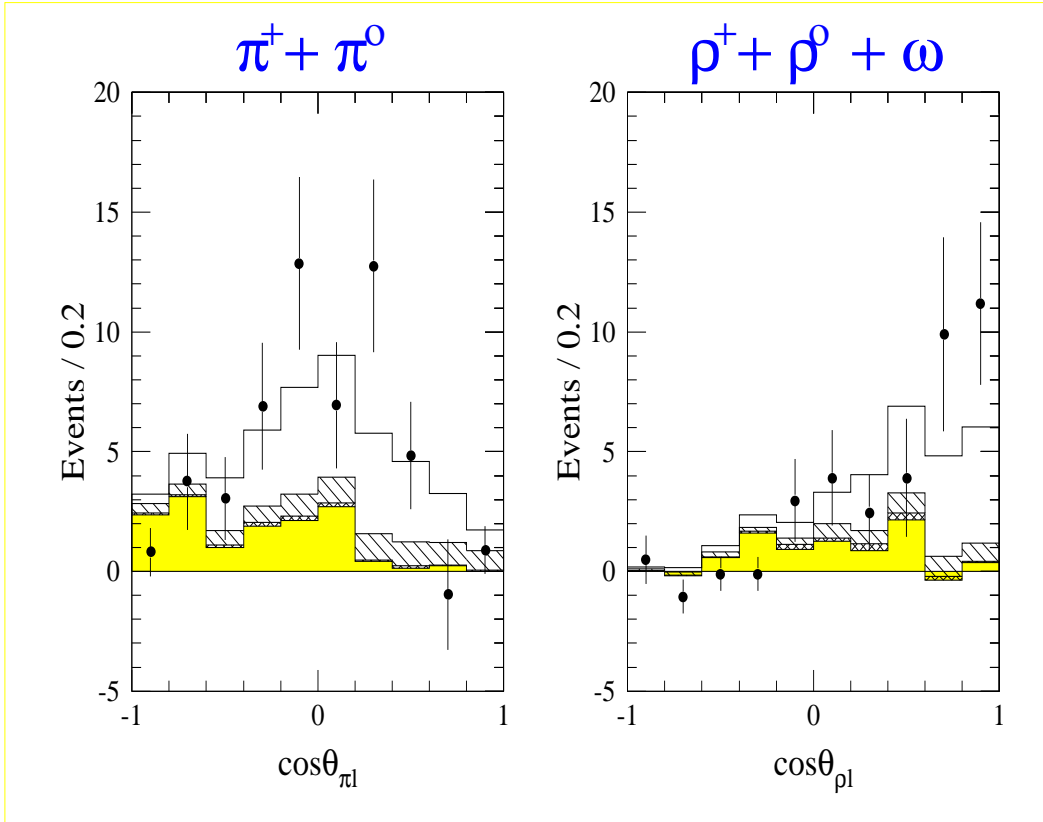


Figure 27: The $\cos\theta_{\pi\ell}$ (left) and $\cos\theta_{\rho\ell}$ (right) distributions where the various components have the same meaning as for Fig. 25.

Model	Prediction	CLEO II
ISGW	4.0	$1.70^{+0.81}_{-0.50} \pm 0.58^{+0.00}_{-0.34}$
WSB	3.0–4.3	$2.39 \pm^{+0.81}_{-0.50} \pm 0.58^{+0.00}_{-0.34}$

Table 5: Predictions and experimental results for the ratio of the $b \rightarrow ul\nu$ rates $\Gamma(B^0 \rightarrow \rho^-\ell^+\nu)/\Gamma(B^0 \rightarrow \pi^-\ell^+\nu)$.

5 Summary and the Future

The power of the CLEO II detector to reconstruct charged and neutral particles with high efficiency and good resolution, coupled with the increased luminosity of CESR, has allowed CLEO to probe deeply into our understanding of heavy

flavor physics. The first observation of exclusive $b \rightarrow u\ell\nu$ decays bodes well for our ability to measure V_{ub} , which is crucial to testing the entire CKM description of \mathcal{CP} Violation. Meanwhile, in the $b \rightarrow c$ sector, the combination of precise measurements of the “baffling” semileptonic and hadronic branching fractions may be pointing towards a problem in the theoretical treatment of heavy flavor decays. The large CLEO charm sample has allowed for the observation of rare phenomena in the D_s^+ system like the observation of isospin violation and purely leptonic decays. Meanwhile, charmed baryons continue to be a laboratory for testing our understanding of the relative contributions of various quark level decay diagrams.

There are a series of improvements planned which will ensure the increased productivity of CLEO. CESR upgrades³¹ will result in a doubling of the luminosity in 1995 with plans to exceed a luminosity of $10^{33} \text{ cm}^{-2}\text{s}^{-1}$, i.e. in the range of a B Factory, towards the end of this century. As for CLEO, a silicon vertex detector will be installed in the fall of 1995. This will not only improve tracking in general but, in particular, will improve the resolution on the crucial $D^{*+} - D^0$ mass difference by a factor of two or three. As well, the ability to reconstruct detached vertices will open up much of the physics associated with the long-lived D^+ . The CLEO III era³² will begin in 1997 with the installation of a new silicon vertex detector and a new drift chamber. Also planned is the installation of a Ring Imaging Cherenkov Counter (RICH) for much improved particle identification. The CsI calorimeter could be said to have revolutionized the physics potential of CLEO by making available a vast number of new channels involving photons (and, hence, the π^0), and the RICH could have a similarly profound impact on the physics reach of CLEO. Some of the physics gains that are made available to CLEO through better particle identification include:

- separating $B \rightarrow K^-\pi$ from $B \rightarrow \pi^-\pi$. This is crucial if one wants to use the integrated rates to extract angles of the unitarity triangle.
- separating $B^- \rightarrow D^0K^-$ from $B^- \rightarrow D^0\pi^-$. $B \rightarrow D^0K$ decays offer an intriguing way to measure an angle of the unitarity triangle³³ but the signal is swamped by the CKM favored $D^0\pi$ channel.
- separating $B \rightarrow \rho\gamma$ from $B \rightarrow K^*\gamma$. Measuring the ratio of these two rates was once touted as the best way to get to $|V_{ts}/V_{td}|$ and measuring either rate will give information pertinent to $b \rightarrow u$ decays.

- separating $D^+ \rightarrow \rho^0 \ell^+ \nu$ from $D^+ \rightarrow \bar{K}^{*0} \ell \nu$. The hope is that the form factors measured in this Cabibbo-suppressed semileptonic D^+ decay can be used, in lieu of theoretical models, in calculations involving $b \rightarrow u$ transitions.

These improvements will ensure that CLEO remains a “top” player in heavy quark physics well into the next century.

References

- [1] The papers describing these results in much more detail, and giving the relevant references to other results and to theoretical predictions, can be accessed from the Cornell Wilson Lab home page on the World Wide Web. The URL is <http://w4.lns.cornell.edu/public/PUBLIC.html>. The relevant links are **CLNS reports**, which are essentially the papers as submitted to the journals, and **conference papers**, where the papers submitted to the 1995 summer conferences can be found.
- [2] CLEO Collaboration, Y. Kubota *et al.*, Nucl. Inst. Methods, **A320**, 66 (1992).
- [3] CLEO Collaboration, K. Edwards *et al.*, Phys. Rev. Lett. **74**, 3331 (1995).
- [4] CLEO Collaboration, T. Miao *et al.*, Phys. Lett. **B323**, 219 (1994); G. Crawford *et al.*, Phys. Rev. Lett. **75**, 624 (1995).
- [5] CLEO Collaboration, R. Ammar *et al.*, Phys. Rev. Lett. **74**, 3534 (1995).
- [6] CLEO Collaboration, J. Alexander *et al.*, Phys. Rev. Lett. **74**, 3113 (1995).
- [7] CLEO Collaboration, A. Bean *et al.*, CLEO CONF 93-8, (1993).
- [8] P. Cho and M. B. Wise, Phys. Rev. **D49**, 6228 (1994), and (presumably) Mark Wise’s contribution to these proceedings.
- [9] The BaBar Technical Design Report, SLAC-R-95-457, (1995).
- [10] CLEO Collaboration, D. Acosta *et al.*, Phys. Rev. **D49**, 5690 (1994).
- [11] Particle Data Group, L. Montanet *et al.*, Phys. Rev. **D50**, S1 (1994).
- [12] CLEO Collaboration, D. Gibaut *et al.*, CLNS 95/1354, submitted to Phys. Rev. **D**.
- [13] G. Martinelli, “ D - and B -Meson Phenomenology from Lattice QCD,” CERN-TH/95-116, (1995).

- [14] S. Capstick and S. Godfrey, Phys. Rev. **D41**, 2856 (1990).
- [15] CLEO Collaboration, M. S. Alam *et al.*, Phys. Rev. **D50**, 43 (1994).
- [16] For a review, see J. D. Richman and P. R. Burchat, “Leptonic and Semileptonic Decays of Charm and Bottom Hadrons,” UCSB-HEP-95-08, (1995).
- [17] CLEO Collaboration, P. Avery *et al.*, Phys. Lett. **B337**, 405 (1994); F. Butler *et al.*, Phys. Lett. **B324**, 255 (1994).
- [18] A. N. Kamal *et al.*, Phys. Rev. **D49**, 1330 (1994).
- [19] CLEO Collaboration, P. Avery *et al.*, Phys. Rev. Lett. **68**, 1279 (1992).
- [20] CLEO Collaboration, R. Balest *et al.*, Phys. Rev. **D52**, 2661 (1995).
- [21] I. Bigi *et al.*, Phys. Lett. **B323**, 408 (1994).
- [22] E. Bagan *et al.*, Phys. Lett. **B342**, 362 (1995).
- [23] CLEO Collaboration, D. M. Asner *et al.*, CLNS95/1338, submitted to Phys. Rev. **D**.
- [24] D. London, “CP Violation in the B System: What’s Old, What’s New?,” **hep-ph/9406412**, (1994).
- [25] CLEO Collaboration, M. S. Alam *et al.*, Phys. Rev. Lett. **74**, 2885 (1995).
- [26] ARGUS Collaboration, H. Albrecht *et al.*, Phys. Lett. **B234**, 409 (1990); **B255**, 297 (1991).
- [27] CLEO Collaboration, R. Fulton *et al.*, Phys. Rev. Lett. **64**, 16 (1990); J. Bartelt *et al.*, Phys. Rev. Lett. **71**, 4111 (1993).
- [28] CLEO Collaboration, B. Barish *et al.*, Phys. Rev. **D51**, 1014 (1995).
- [29] M. Wirbel *et al.*, Zeit. Phys. **C29**, 637 (1985).
- [30] N. Isgur *et al.*, Phys. Rev. **D39**, 799 (1989).
- [31] “The CESR/CLEO Upgrade Project,” CLNS93/1265, (1993).
- [32] “The CLEO III Detector: Design and Physics Goals,” CLNS94/1277, (1994).
- [33] M. Gronau and D. Wyler, Phys. Lett **B265**, 172 (1991).